J. Fluid Mech. (2007), *vol.* 573, *pp.* 417–456.
doi:10.1017/S0022112006003892 Printed in the United Kingdom

Characteristics of the wind drift layer and microscale breaking waves

M. H. KAMRAN SIDDIQUI† AND MARK R. LOEWEN‡

Department of Civil and Environmental Engineering, University of Alberta, 3-133 Markin/CNRL Natural Resources Engineering Facility, Edmonton, Alberta, Canada T6G 2W2

(Received 21 January 2004 and in revised form 24 August 2006)

An experimental study, investigating the mean flow and turbulence in the wind drift layer formed beneath short wind waves was conducted. The degree to which these flows resemble the flows that occur in boundary layers adjacent to solid walls (i.e. wall-layers) was examined. Simultaneous DPIV (digital particle image velocimetry) and infrared imagery were used to investigate these near-surface flows at a fetch of 5.5 m and wind speeds from 4.5 to 11 m s^{-1}. These conditions produced short steep waves with dominant wavelengths from 6 cm to 18 cm. The mean velocity profiles in the wind drift layer were found to be logarithmic and the flow was hydrodynamically smooth at all wind speeds. The rate of dissipation of turbulent kinetic energy was determined to be significantly greater in magnitude than would occur in a comparable wall-layer. Microscale breaking waves were detected using the DPIV data and the characteristics of breaking and non-breaking waves were compared. The percentage of microscale breaking waves increased abruptly from 11 % to 80 % as the wind speed increased from 4.5 to 7.4 m s^{-1} and then gradually increased to 90 % as the wind speed increased to 11 m s^{-1}. At a depth of 1 mm, the rate of dissipation was 1.7 to 3.2 times greater beneath microscale breaking waves compared to non-breaking waves. In the crest–trough region beneath microscale breaking waves, 40 % to 50 % of the dissipation was associated with wave breaking. These results demonstrated that the enhanced near-surface turbulence in the wind drift layer was the result of microscale wave breaking. It was determined that the rate of dissipation of turbulent kinetic energy due to wave breaking is a function of depth, friction velocity, wave height and phase speed as proposed by Terray *et al.* (1996). Vertical profiles of the rate of dissipation showed that beneath microscale breaking waves there were two distinct layers. Immediately beneath the surface, the dissipation decayed as $\zeta^{-0.7}$ and below this in the second layer it decayed as ζ^{-2}. The enhanced turbulence associated with microscale wave breaking was found to extend to a depth of approximately one significant wave height. The only similarity between the flows in these wind drift layers and wall-layers is that in both cases the mean velocity profiles are logarithmic. The fact that microscale breaking waves were responsible for 40 %–50 % of the near-surface turbulence supports the premise that microscale breaking waves play a significant role in enhancing the transfer of gas and heat across the air–sea interface.

† Present address: Department of Mechanical and Industrial Engineering, Concordia University, 1455 de Maisonneuve Blvd. West, Montreal, Quebec, H3G 1M8, Canada.

‡ Author to whom correspondence should be addressed: mrloewen@ualberta.ca.

1. Introduction

When the wind blows over a water surface a complex flow is generated beneath the water surface. At very low wind speeds, prior to the appearance of surface waves, the flow is comprised of a shear current, the so-called wind drift current. As the wind speed increases surface waves appear and the flow becomes more complex as wave-induced motions are superimposed on the wind drift current. At higher wind speeds, surface wave breaking occurs and an extremely complex flow is produced as the wind drift current, wave orbital motions and turbulence are superimposed. In the absence of convective motions, the dominant sources of turbulence in the wind drift layer are wave breaking and shear production.

The properties of the flow in the wind drift layer are of interest to oceanographers, limnologists and engineers for a number of reasons. Mixing in the upper ocean, the transfer of gas, heat and momentum across the air–water interface, the movement and dispersion of oil slicks and the properties of the surface wave field are all influenced by the characteristics of this near-surface flow. Study of the aqueous boundary layer has proved challenging because of the difficulty of making accurate near-surface measurements beneath a fluctuating air–water interface, particularly in natural water bodies. As a result, much of our understanding of the wind drift layer has been gained through controlled laboratory studies.

In this paper, we report on a series of experiments conducted in a laboratory wind wave tank. One objective of this study was to investigate the time-averaged properties of the flow in the wind drift layer. Of particular interest was the degree to which these aqueous boundary layers resemble the boundary layers formed adjacent to solid walls. A second objective of the study was to determine the influence of microscale wave breaking on the near-surface turbulence. Microscale breaking waves are defined as short wind waves that break without entraining air. These small-scale breaking waves generate near-surface turbulence that has been shown to enhance the transfer of gas and heat across the air–water interface (Siddiqui *et al.* 2004; Zappa *et al.* 2004). Because of their wide spread occurrence on the ocean surface, it has been speculated that these microbreakers may play an important role in controlling air–sea gas and heat fluxes (Banner & Peregrine 1993; Melville 1996).

2. Previous studies

2.1. *Mean flow*

Previous studies of the aqueous boundary layer have drawn on the vast body of work on boundary layers formed adjacent to solid walls. The flow regime in solid wall boundary layers is classified as hydrodynamically smooth, in transition, or rough. In all three flow regimes a logarithmic layer is found to exist in which the velocity follows a logarithmic equation of the form,

$$\frac{U(z)}{u_*} = \frac{1}{\kappa} \ln\left(\frac{z}{z_o}\right), \tag{1}$$

where, $U(z)$ is the mean horizontal velocity, z is the distance from the wall, u_* is the friction velocity, κ is the Kármán constant ($\kappa = 0.4$–0.41) and z_o is the roughness length. Measurements of the mean velocity profile in the logarithmic layer are typically used to determine the value of u_* and z_o.

One important difference between solid wall boundary layers and aqueous boundary layers is the boundary condition at the surface. At a solid wall, the velocity must be

zero because of the no-slip boundary condition. However, the boundary condition that must be satisfied at the water surface in an aqueous boundary layer is that the velocity defect must be zero. The velocity defect is defined as, $U_s - U(z)$ where U_s is the average wind-induced surface velocity. Note that when (1) is applied to an aqueous boundary layer, $U(z)$ is replaced by the velocity defect. Keulegan (1951) was one of the first to measure the magnitude of the wind-induced surface velocity and he found that it had a magnitude of approximately 3.3 % of the wind speed. Subsequent experimental investigations have confirmed that the wind-induced surface velocity is typically 3–4 % of the wind speed (e.g. Van Dorn 1953; Bye 1965; Shemdin 1972).

Bye (1965) and Churchill & Csanady (1983) conducted field studies of the aqueous boundary layer and found that they were logarithmic. Shemdin (1972), Wu (1975) and Lin & Gad-el-Hak (1984) also observed logarithmic velocity profiles during their wind wave tank studies. In these laboratory and field studies, the magnitude of the friction velocities ranged from 0.1 to 1.5 cm s^{-1}, but was typically of the order 1 cm s^{-1}. The roughness heights in the aqueous boundary layer were found to vary in the range of 0.05–0.3 cm, with the exception of Churchill & Csanady (1983) who estimated values of $z_o = 12$ to 50 cm. However, when Bourassa (2000) reanalysed the velocity profile data used by Churchill & Csanady (1983), he predicted z_o values in the range 0.4 to 1.5 cm.

Cheung & Street (1988; hereinafter referred to as CS) studied the aqueous boundary layer formed beneath wind-generated waves and wind-ruffled mechanical waves in a wind wave tank. Beneath wind waves, they observed logarithmic velocity profiles at all windspeeds. However, at most wind speeds the mean velocity profiles had slopes less than 2.5 indicating that the Kármán constant was larger than 0.4. Their estimates of u_* ranged from 0.21 to 2.75 cm s^{-1}. At wind speeds greater than 3.2 m s^{-1}, they found that the flow in the aqueous boundary layer was hydrodynamically rough. This differed from earlier studies in which the aqueous boundary layer was found to be hydrodynamically smooth (Wu 1975) or in the transition regime (Bye 1965; Lin & Gad-el-Hak 1984).

Sullivan, McWilliams & Melville (2004) carried out direct numerical simulations that included a stochastic model of the effects of wave breaking on the oceanic boundary layer. Their model predicted that profiles of the horizontal mean velocity shifted as the breaker forcing was increased and this was interpreted as being equivalent to an increase in the surface roughness. Contrary to CS's finding, they predicted that the slope of the mean velocity profiles was always 2.5 (i.e. that the von Kármán constant was equal to 0.4).

2.2. *Turbulence beneath surface waves*

2.2.1. *Field studies*

A number of field studies have demonstrated that the near-surface turbulence is enhanced by wave breaking (Agrawal *et al.* 1992; Anis & Moum 1995; Terray *et al.* 1996; Soloviev & Lukas 2003; Gemmrich & Farmer 2004). Agrawal *et al.* (1992) found that the rate of dissipation of turbulent kinetic energy, ε, could be up to a factor of 100 greater than the value predicted by wall-layer theory. A time series of ε revealed that the turbulence was highly intermittent with maximum values that were in excess of 14 times the mean value. Based on these findings, they hypothesized that the background level of turbulence that is close to wall-layer estimates was produced either by microscale wave breaking or shear production in the wind drift layer. The source of the intense intermittent events that produced spikes in the value of ε was postulated to be large-scale breaking waves (i.e. whitecaps).

Terray *et al.* (1996) observed dissipation rates that were one to two orders of magnitude greater than wall-layer values. Their observations suggested that the wave-stirred near-surface region is comprised of three layers. The uppermost layer has a depth approximately equal to the significant wave height wave where ε is very high and approximately constant. Below this is an intermediate layer in which ε is still larger than wall-layer values and decays as z^{-2}. The thickness of this layer is a function of the significant wave height and the wave age (i.e. c/u_*, where c is the phase speed of the dominant waves). Below this is a layer in which the values of ε asymptote to wall-layer values.

Gemmrich & Farmer (2004) observed dissipation rates that were several hundred times larger than wall-layer values in the open ocean. Values of ε measured beneath the crests of breaking waves were approximately 1.6 times larger than beneath the troughs. In the crest region above the mean water line, ε varied as $z^{-2.3}$ and below this level it was approximately constant. An increase in turbulence levels beneath the forward face of breaking waves was observed up to a quarter of a wave period prior to air entrainment. They concluded that the occurrence and magnitude of this pre-breaking turbulence was consistent with direct wave–turbulence interactions (Thais & Magnaudet 1996), associated with microscale wave breaking.

2.2.2. *Laboratory studies*

CS made laser-Doppler anemometer (LDA) measurements in a wind wave tank at depths below the troughs of pure wind waves and wind-ruffled mechanical waves at a fetch of 13 m and wind speeds up to 13.1 m s^{-1}. The wave and turbulent velocities were separated using a linear filtration method. Friction velocities for the aqueous boundary layer were computed by extrapolating profiles of the Reynolds stress to the water surface. They argued that the waves affect the mean flow directly, leading to a change in the slope of the mean velocity profiles and that there is a transfer of energy from the wave field to the mean flow. Their observations led to the conclusion that the presence of waves increased the kinetic energy of the mean flow. They also found that the turbulent intensity profiles observed beneath wind waves were similar to those observed in flows over flat plates, but that the profiles beneath the mechanical waves were unusual. These observations led them to conclude that there was a coupling of the turbulence and the wave-induced motions beneath the wind-ruffled mechanically generated waves.

Jiang, Street & Klotz (1990) reanalysed CS's wind wave data using a nonlinear streamfunction to separate the wave and turbulent velocities. The nonlinear wave–turbulence separation technique produced estimates of the root mean square turbulent velocities, turbulent shear stresses and turbulent kinetic energy production at all wind speeds that agreed with CS's estimates. Their data analysis showed that the coherence between the wave and turbulent velocities was very high at certain frequencies and they attributed this to wave–turbulence interactions. They conclude that these interactions lead to considerable energy transfer between the mean, turbulent and wave-induced velocity components.

Thais & Magnaudet (1996) also studied the structure of the turbulent flow beneath wind waves and wind-ruffled mechanical waves in a wind wave tank. They made LDA measurements of the three components of the instantaneous velocity at depths below the wave troughs at a fetch of 26 m and at wind speeds up to 7.8 m s^{-1}. The primary motivation for their work was to investigate whether significant wave–turbulence interactions occur beneath surface gravity waves. In particular, they were interested in determining how similar the turbulent flow generated beneath wind-driven

water surfaces is to wall-layer flows. Thais & Magnaudet (1996) separated the wave and turbulent velocities using a nonlinear triple decomposition method described in detail in Thais & Magnaudet (1995). Their most significant finding was that the turbulent kinetic energy and its dissipation rate reached levels much higher than values found in wall-bounded flows. This was the first laboratory study to show that the rate of dissipation of turbulent kinetic energy could be significantly enhanced, compared to wall-layer values, beneath wind waves at moderate wind speeds. The turbulent velocity spectra had a slope of -3 at frequencies greater than the dominant wave frequency and they concluded that this was an indication of dynamic wave–turbulence interactions. Below the wave troughs at all wind speeds, turbulent production by the mean shear was negligible and turbulent diffusion and dissipation were roughly in balance. Thais & Magnaudet (1996) state that this balance cannot explain the high levels of turbulence that were observed and they concluded that intense wave–turbulence interactions leading to the production of turbulence must occur in the water above the wave troughs. They found that the frequency of near-surface bursting events was dramatically increased beneath the wave crest and they suggested that the generation of such high turbulence near the crests of the dominant wave could be attributed to vorticity generation by capillary ripples or micro-breaking.

2.3. *Microscale wave breaking*

Banner & Phillips (1974) introduced the term 'micro-breaking' to describe the breaking of short wind waves without air entrainment. Micro-breakers, now referred to as microscale breaking waves, occur at low to moderate wind speeds (i.e. 4 to $12\,\mathrm{m\,s^{-1}}$) and are typically $O(0.1\text{–}1)\,\mathrm{m}$ in length, a few centimetres in amplitude, and have a bore-like crest directly preceded by parasitic capillary waves riding along the forward face (Jessup, Zappa & Yeh 1997). On the ocean surface, microscale breaking waves occur much more frequently than large-scale breaking waves, leading some workers to suggest that microscale wave breaking may be important in controlling the flux of heat, gas and momentum across the interface (Banner & Peregrine 1993; Melville 1996). This has been confirmed by two sets of laboratory wind wave experiments. Zappa, Asher & Jessup (2001) showed that microscale wave breaking is the physical process that determines the gas transfer rate at low to moderate wind speeds and Siddiqui *et al.* (2001, 2004) found that the turbulent wakes produced by microscale breaking waves enhance air–water heat and gas transfer rates.

Peirson & Banner (2003) investigated the flow beneath microscale breaking waves using high-resolution digital particle image velocimetry (DPIV) measurements. Microscale breaking waves were detected using a scheme based on the local wave slope. They observed high values of the vorticity and surface convergence at the leading edge of the spilling region. They argued that these regions of localized convergence were produced by subduction of the fluid beneath the spilling region.

Zappa *et al.* (2001, 2004) reported on laboratory wind wave experiments conducted using simultaneously sampled and collocated infrared (IR) and wave slope imagery. IR imagery was used to detect microscale breaking waves. It was found that the fractional area coverage of the wakes (A_B) generated by microscale breaking waves was correlated with the air–water gas and heat transfer velocities. The disruption of the skin layer was shown to coincide with waves that have a steep forward face and dimpled bore-like crest. Zappa *et al.* (2004) measured the local heat transfer velocities inside and outside the wakes generated by microscale breaking waves and found that on average, the transfer velocity was enhanced by a factor of 3.5 inside the wakes.

They also estimated that up to 75 % of the transfer across the air–water interface was contributed by microscale wave breaking. Hence, they concluded that in their experiments, microscale wave breaking was the physical process that controlled the transfer rate at low to moderate wind speeds.

Siddiqui *et al.* (2001) presented preliminary results from a laboratory investigation of the flow fields beneath microscale breaking waves using simultaneously sampled and collocated IR imagery and DPIV. They found that the wakes generated by microscale breaking waves were typically produced by a series of near-surface vortices that form behind the leading edge of the breaker. Strong correlations were observed between the near-surface vorticity and both A_B and the local heat transfer velocity. The main conclusion was that the wakes produced by microscale breaking waves were regions of high near-surface vorticity that were in turn responsible for enhancing air–water heat transfer rates.

Siddiqui *et al.* (2004) investigated the properties of near-surface coherent structures or eddies and their influence on air–water gas transfer. A coherent structure or an eddy is defined as a connected large-scale turbulent fluid parcel with a phase-correlated vorticity over its spatial extent. A new parameterization for the air–water gas transfer velocity based on the surface renewal model was developed. The results indicated that 60 % of the total air–water gas flux, at all wind speeds, was due to surface renewal produced by the observed near-surface coherent structures.

In this paper, we report on results from a more detailed analysis of the data from the set of experiments discussed by Siddiqui *et al.* (2001, 2004). In § 2, the experimental set-up and procedures are described. In § 3, the properties of the flow in the wind drift layer are analysed and discussed. In § 4, the characteristics of microscale breaking and non-breaking waves are compared, and the impact of microscale wave breaking on the near-surface flow is discussed.

3. Experimental methods

A series of experiments were conducted in a wind-wave flume at Harris Hydraulics Laboratory, University of Washington, Seattle, WA. The flume is 9.2 m long, 1.17 m wide and the water depth during the experiments was maintained at 87 cm. A horsehair beach was placed at the downstream end of the tank to absorb wave energy. A centrifugal fan installed on the upstream end of the tank produced wind speeds up to approximately $12\,\mathrm{m\,s^{-1}}$. The experimental set-up and instrumentation are shown schematically in figure 1. Measurements were made at a fetch of 5.5 m at wind speeds ranging from $4.5\,\mathrm{m\,s^{-1}}$ to $11.0\,\mathrm{m\,s^{-1}}$. The water surface was vacuumed at the beginning of each day of the experiments in order to keep it clean. Wind speed at a height of 60 cm and bulk air and water temperatures were also measured for each experimental run. The data were sampled at a rate of 100 Hz per channel using an eight-channel A/D board. To obtain a strong thermal signature for the IR measurements, the water was heated prior to each experimental run and the average air–water temperature difference ranged from 7 °C to 11 °C. Details of the experimental conditions are provided in table 1. To help facilitate comparisons to field data, the wind speed measurements were extrapolated to a height of 10 m using empirical expressions from Donelan (1990) and Smith (1988). The values of U_{10} range from 6.6 to $18.3\,\mathrm{m\,s^{-1}}$ and are also given in table 1.

Digital particle image velocimetry (DPIV) was used to measure the two-dimensional velocity field beneath the wind waves in a plane parallel to the wind and bisecting the water surface, as shown in figure 1. The DPIV light source was a 500 mW, 678 nm

U_∞ (m s^{-1})	4.5	6.1	7.4	8.5	11.0
U_{10} (m s^{-1})	6.3	9.1	11.5	13.5	18.6
f_d (Hz)	5.2	4.10	3.7	3.5	3.0
λ_d (cm)	5.8	9.3	11.4	12.8	17.6
H_{rms} (cm)	0.29	0.55	0.75	0.89	1.19
H_s (cm)	0.43	0.82	1.11	1.25	1.76
$\langle S^2 \rangle$	0.012	0.017	0.020	0.022	0.025
T_{air} (°C)	23.3	27.7	24.2	27.7	26.6
T_{water} (°C)	34.2	35.0	34.6	34.4	34.6

TABLE 1. Summary of environmental parameters for different experimental runs. U_∞, wind speed measured at a height of 60 cm; U_{10}, wind speed at a height of 10 m; f_d, the dominant wave frequency; λ_d, the dominant wavelength; H_{rms}, the r.m.s. wave height; H_s, the significant wave height; $\langle S^2 \rangle$, mean-square wave slope; T_{air}, the average air temperature; T_{water}, the average water temperature. The dominant wavelength was computed from the linear dispersion relationship.

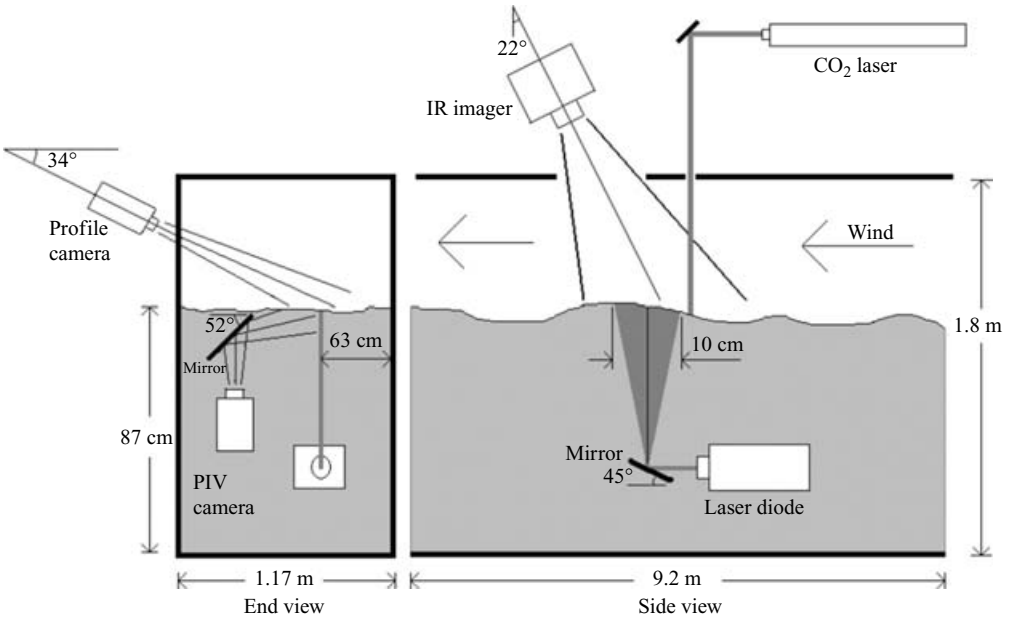

FIGURE 1. Schematic of the experimental set-up.

wavelength laser diode (Magnum 500 SP, Lasiris, Montreal, Quebec). The laser diode was equipped with a light head that created a uniform light sheet of approximately 200 μm thickness; with a 20° fan angle. A progressive scanning full frame 8-bit CCD camera (Pulnix TM-9701, Sunnyvale, CA) with a resolution of 768×484 pixels was used to image the flow field. The field of view of the camera was 8.4 cm wide and 6.2 cm high. The camera was connected to a PC equipped with a digital frame grabber (Road Runner, Bitflow, Woburn, MA) that acquired 8-bit digital images at a rate of 30 Hz. To optimize the results, both the diode laser and the DPIV camera were placed under the water in waterproof housings (figure 1). The water was seeded with silver-coated glass spheres, with a mean diameter of 15 μm and a specific gravity of 1.65 (Potters Industries, Paoli, PA). These glass spheres were used as tracer particles for

the DPIV measurements. A four-channel digital delay generator (DG 535, Stanford Research Systems, Palo Alto, CA) was used to control the timing and duration of the light pulses. For these experiments, we set the pulse duration and the pulse separation at 1.0 ms and 2.0 ms, respectively.

A problem encountered when DPIV is used to measure the near-surface velocity field is that in many of the DPIV images, reflected seed particles appear above the air–water interface, making it impossible to locate the true position of the interface. This is a serious problem since accurately locating the interface in the DPIV images is a crucial step in reliably estimating the near-surface velocities. In order to locate the interface in the DPIV images, the surface wave profiles were measured using a technique similar to that reported by Banner & Peirson (1998) and Law, Khoo & Chew (1999). This technique is based on the fact that the laser light sheet is visible only in the water because of the high reflectivity of the seed particles. A second CCD camera (Model 2122, Cohu Electronics, San Diego, CA) with a resolution of 768×494 pixels operating in the interlaced mode was used to image the surface wave profile, where the laser light sheet intersects the water surface. The camera was mounted on a stand 43.8 cm above the mean water level looking down at an angle of 34° with respect to the horizontal (figure 1). The surface wave profile images were recorded on videotape in standard NTSC RS-170 format using a VHS video tape recorder (HS-4790, Mitsubishi, Cypress, CA). The profile images were subsequently digitized using a Pentium-class personal computer equipped with a frame grabber (Meteor II, Matrox Electronic Systems, Dorval, Quebec) at a resolution of 640×480 pixels.

The water surface in the profile images was located on the basis of the difference in the grey-scale values in the air and water since in the water the light sheet is brighter owing to the reflection of the seed particles. The uncertainty in computing the surface wave profile in the profile images was estimated to be ± 0.3 mm. The surface wave profile data were then imported into the corresponding DPIV image and the total error in locating the water surface in the DPIV images was estimated to be ± 0.5 mm. To validate the water surface profile measurements, wave properties computed from the profile data were compared with the surface displacement data from the wave gauges in a separate set of experiments. The comparison showed that the differences in the root-mean-square (r.m.s.) wave height were <3 % and the differences in the r.m.s. wave slope were <8 %, confirming that the profile images could be used to measure the water surface profile accurately. Complete details of the wave profile–wave gauge comparison are reported in Siddiqui *et al.* (2001).

The water surface temperature measurements were made using an infrared imager (Radiance HS Raytheon TI Systems, Dallas, TX) with a resolution of 256×256 pixels. This imager is sensitive to radiation in the 3–5 μm wavelength band, and its optical depth in water is approximately 10 μm. The IR imager was mounted on top of the tank looking down at an incidence angle of 68°, with a field of view of approximately 34.3 cm × 34.3 cm (figure 1). The IR imager has a digital output with 12-bit resolution and an internal flag assembly to correct for any residual fixed pattern noise (non-uniformity) existing in the focal plane array. The imager was connected to a PC equipped with a digital frame grabber (Road Runner, Bitflow, Woburn, MA) that acquired 12-bit digital images at 30 Hz. For each experimental run 900, 12-bit digital IR images and 900, 8-bit DPIV images were acquired at a rate of 30 Hz. Twenty experimental runs were conducted at each wind speed.

Simultaneous sampling of the DPIV, profile and IR images was achieved by synchronizing all three cameras. The vertical sync signal was stripped from the composite analogue video signal of the profile camera and used to synchronize the DPIV camera

and the IR imager. The delay generator was used to trigger the start of the data acquisition. A rigid frame with horizontal and vertical scales mounted on it, was used to determine the fields of view of the DPIV and profile cameras and to collocate them. The frame was mounted such that the horizontal and vertical scales were in the fields of view of both cameras. The resulting digital images captured by both cameras were used to convert the horizontal and vertical cell dimensions of each camera into actual distance and to collocate the field of view of both cameras. The location of the field of view of the DPIV camera was located in the IR camera's field of view by placing a metal strip at the location where the plane of the DPIV field of view intersected the water surface. The metal strip appeared as a straight line in the IR images, thus locating the DPIV plane. The uncertainty in locating the DPIV field of view in the IR images was estimated to be ± 3 mm.

The velocity field was estimated by computing a cross-correlation between the interrogation window (32×32 pixels) in the first image and the corresponding search window (64×64 pixels) in the second image. A 50 % window overlap was used in order to increase the nominal resolution of the velocity field to 16×16 pixels and a spatial resolution of $1.75\,\text{mm} \times 2.07\,\text{mm}$. With this resolution, the closest measurements relative to the water surface were, on average, 1 mm below the surface. Velocity vectors located above the interface were discarded. A scheme was developed to identify the spurious vectors and then correct them using a local median test (see Siddiqui *et al.* 2001). Typically, fewer than 4 % of the velocity vectors were spurious. The vorticity was computed using a central difference scheme. The errors in the velocity and vorticity measurements were estimated to be $1.2\,\text{cm}\,\text{s}^{-1}$ and $2.7\,\text{s}^{-1}$, respectively.

4. Wind drift layer

4.1. *Wave properties*

The root-mean-square (r.m.s.) wave height (H_{rms}), significant wave height (H_s), dominant wave frequency (f_d) and the mean-square wave slope ($\langle S^2 \rangle$) were computed from the surface wave profile data. The dominant wavelength (λ_d) was estimated from the deep-water dispersion relationship and these data are presented in table 1. The r.m.s. wave slope was computed from the surface wave profiles which had been smoothed with a low-pass filter with a cut-off wavelength of 6 mm. As the wind speed increased from 4.5 to $11\,\text{m}\,\text{s}^{-1}$, the r.m.s. wave height and dominant wave frequency varied from 0.29 to 1.19 cm and 5.2 to 3.0 Hz, respectively.

4.2. *Surface drift velocity*

The Lagrangian surface drift (U_{SL}) was measured by tracking a circular heated patch that was generated at the water surface by a carbon dioxide (CO_2) laser (Synrad H48-2-28S 25 W, 10 μm wavelength). The laser was pulsed for 40 ms and produced a 2 cm diameter heated circular patch on the water surface once every second. The heated patch was tracked using IR imagery and the coordinates of the centroid of the patch were used to estimate U_{SL}. The values of U_{SL} averaged over ~300 patches at each wind speed, are given in table 2. The magnitude of the Lagrangian surface drift velocity ranged from 2.1 % to 2.5 % of the wind speed (see table 2), which is comparable to previous measurements (Peirson 1997; CS). The Stokes drift (U_{Stokes}) induced by the surface waves was estimated from,

$$U_{Stokes} = \int E(\sigma) k \sigma \, \mathrm{d}\sigma \tag{2}$$

U_∞ (m s^{-1})	4.5	6.1	7.4	8.5	11.0	E_s (%)
U_{SL} (cm s^{-1})	11.30	15.28	16.81	19.41	22.69	± 10
U_{SL}/U_∞ (%)	2.5	2.5	2.3	2.3	2.1	
U_{Stokes} (cm s^{-1})	0.36	0.68	0.99	1.1	1.36	
U_s (cm s^{-1})	10.94	14.60	15.82	18.31	21.33	
u_*(cm s^{-1})	0.32	0.34	0.46	0.48	0.63	± 20
$z_o \times 10^{-4}$ (cm)	1.38	0.12	2.64	1.4	3.4	± 70
δ_v (cm)	0.13	0.12	0.087	0.083	0.063	

TABLE 2. Values of U_∞, the wind speed measured at a height of 60 cm; U_{SL}, the Lagrangian surface drift; U_{SL}/U_∞, in per cent; U_{Stokes}, Stokes drift velocity; U_s, surface velocity; u_*, friction velocity; z_o, roughness length; δ_v, thickness of the viscous sublayer; E_s, uncertainty in the various parameters.

where, $E(\sigma)$ is the frequency spectrum of the surface displacement, k is the wavenumber and σ is the intrinsic wave frequency (rad s^{-1}) (Bye 1967). The integration was computed over the entire frequency spectrum of the surface displacement, at each wind speed. The intrinsic wave frequencies were computed from the apparent or measured wave frequencies using the deep-water dispersion relation and the measured values of the surface drift (Mei 1983). The surface velocity (U_s) was then computed by subtracting U_{Stokes} from U_{SL}. The values of U_{Stokes} and U_s are also presented in table 2.

4.3. *DPIV velocity measurements*

The DPIV measurements provide instantaneous velocity fields in a fixed Eulerian coordinate system. In this study, the vertical distance between the two velocity grid points was 2.07 mm. This distance is a factor of two smaller than the r.m.s. wave height at the lowest wind speed and a factor of six smaller than the r.m.s. wave height at the highest wind speed. Therefore, in this coordinate system, at any fixed grid point located in the crest–trough region, the water surface fluctuates above and below this point. Hsu, Hsu & Street (1981) investigated the flow over and beneath mechanically generated water waves. They argued that time-averaged quantities do not exist in a useful form at a fixed position in the crest–trough region because this fixed position is sometimes in the water and sometimes in the air. Therefore, they transformed the fixed Eulerian coordinate system into a wave-following Eulerian system by transforming the vertical coordinate only.

Following Hsu *et al.* (1981), we transformed the velocity data from a fixed Eulerian system to a wave-following Eulerian system. The origin in the wave-following coordinate system was defined as the air–water interface, that is, the vertical coordinate $\zeta = 0$ at the interface and the negative ζ-axis points downwards parallel to the gravity vector. The velocity grid points are 2.07 mm apart vertically and therefore, on average, the first grid point was located at $\zeta = -1.0$ mm. At the highest wind speed (11.0 m s^{-1}), the deepest velocity measurements that were possible in the wave-following coordinate system were 25 mm below the interface. Beneath the troughs of some waves, depths larger than 25 mm were located below the field of view of the DPIV camera, and therefore, the velocity data at all wind speeds were transformed into the wave-following coordinate system only to a maximum depth of $\zeta = -25$ mm.

The mean velocity components were computed by first time-averaging 10 min of instantaneous velocity measurements at a given depth at each grid point in the wave-following coordinate system. Next, these time-averaged velocities were spatially

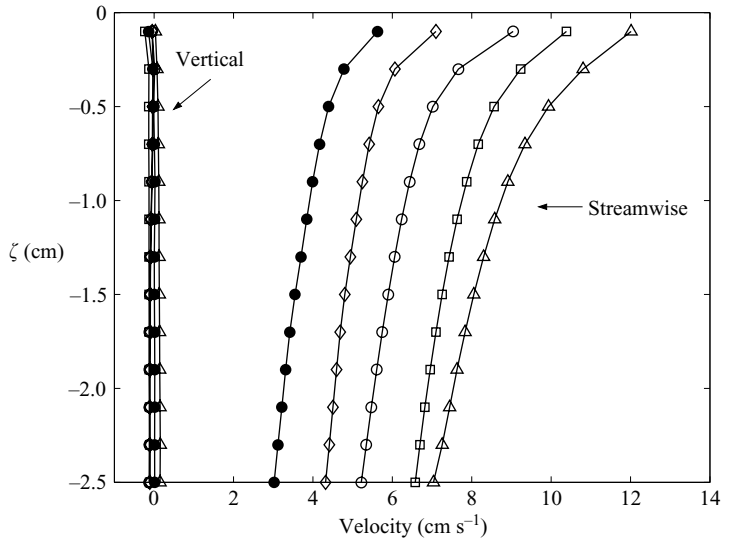

FIGURE 2. Vertical profiles of the streamwise and vertical components of the mean velocity. ●, 4.5 m s^{-1}; ◇, 6.1 m s^{-1}; ○, 7.4 m s^{-1}; □, 8.5 m s^{-1}; △, 11.0 m s^{-1}. ζ is the vertical coordinate in the wave-following system. The mean velocity at a given depth was obtained by time-averaging 10 min of data and spatially averaging over the width of the PIV field of view.

averaging across the DPIV field of view. Therefore, each mean velocity data point was computed by averaging a total of 405 000 velocity measurements (i.e. 600 s × 15 Hz × 45 horizontal grid points). This averaging procedure provided very reliable estimates of the mean velocity components. Vertical profiles of the mean velocity components are shown plotted in figure 2 at five wind speeds. The mean vertical velocity is essentially zero at all wind speeds, indicating that there are no significant systematic errors in the velocity measurements. As expected, the mean horizontal velocity increases with wind speed and decreases monotonically with depth. When these mean velocity profiles were plotted on a semi-logarithmic scale (not shown here), it was evident that a log layer existed at all wind speeds (i.e. U was proportional to $\log(\zeta)$).

4.3.1. *Wave–turbulence decomposition*

Under wind waves, the instantaneous velocity field is typically decomposed into three components using the following equation,

$$u(x,t) = \bar{u} + \tilde{u}(x,t) + u'(x,t), \tag{3}$$

where $\bar{u}$, $\tilde{u}$ and u' are the mean, wave-induced and turbulent components of the instantaneous velocity field, respectively (Benilov, Kouznetsov & Panin 1974). Several methods have been developed for performing this decomposition (CS; Jiang *et al.* 1990; Thais & Magnaudet 1995). These decomposition methods are typically used in studies investigating the interactions between the wave and turbulent components of the velocity, so-called wave–turbulence interactions.

CS decomposed the wave and turbulent velocities using a linear filtration method. Jiang *et al.* (1990) used a nonlinear streamfunction to decompose the wave and turbulent velocities. Thais & Magnaudet (1995) decomposed the wave and turbulent velocities using a nonlinear triple decomposition method. All three methods relied on the assumptions that the waves were two-dimensional and that the waves were non-dispersive.

There are two primary reasons why we chose not apply any of these particular methods to our data set. First, these methods have only been applied to laser-Doppler anemometer velocity data sampled at a rate of 100 to 200 Hz at points located beneath the wave troughs. The sampling rate of our DPIV data was 15 Hz giving a Nyquist frequency of 7.5 Hz, which is too low for resolving the turbulence in the time domain. As a result, it is not obvious how these methods that were designed for use with velocity data with high temporal resolution at a fixed point could be applied to DPIV data with high spatial resolution and poor temporal resolution. The second reason is that the assumptions that the waves are two-dimensional and non-dispersive are questionable for the waves observed in this study. Since the DPIV velocity data have a relatively high spatial resolution, we developed a method for decomposing the wave and turbulent components that uses a spatial filter. This is analogous to applying a linear filtration technique to a time series of velocity data (Benilov *et al.* 1974).

In the present velocity decomposition scheme, the mean velocity components were first subtracted from the instantaneous velocities. The resulting velocity components were designated, u_{wt} and w_{wt}, to indicate that they were comprised of the wave and turbulent velocities. The turbulent velocity component was separated by spatially high-pass filtering u_{wt} and w_{wt}. The cutoff wavenumber of the spatial filter was selected based on the properties of the coherent structures that were detected in the velocity data. A detailed description of the coherent structure detection scheme and their properties is given in Siddiqui *et al.* (2004). Plots of the distributions of the kinetic energy of the coherent structures as a function of wavenumber revealed that the size of the most energetic coherent structures varied from 8 mm to 16 mm at wind speeds of 4.5 and 11 m s^{-1}, respectively. This corresponds to wavenumbers of approximately 800 and 400 rad m^{-1}. Therefore, the cutoff wavenumber of the spatial filter was set at 320 rad m^{1} corresponding to a length scale of 20 mm. This cutoff ensures that none of the energetic coherent structures are removed from the turbulent velocity field by the spatial filter.

A low-pass 9×9 boxcar window with a cutoff wavenumber of 320 rad m^{-1} was selected as the spatial filter. First, u_{wt} and w_{wt} were low-pass filtered using the boxcar filter in order to separate the wave velocity components, $\tilde{u}$ and $\tilde{w}$. Then, the turbulent velocity components were calculated by subtracting $\tilde{u}$ from u_{wt} and $\tilde{w}$ from w_{wt} (i.e. $u' = u_{wt} - \tilde{u}$ and $w' = w_{wt} - \tilde{w}$). These operations are equivalent to high-pass filtering u_{wt} and w_{wt} with a spatial filter with a cutoff wavenumber of 320 rad m^{-1}. Note, that the 32×32 pixel interrogation window used in the DPIV processing spatially low-pass filters the velocity field at 3.5 mm; and therefore, the turbulent velocity components include eddies with length scales from 3.5 mm to 20 mm.

The roll-off of the wavenumber response of the 9×9 boxcar filter is not very steep and as a result, the turbulent velocity field obtained from this filtering process was contaminated to varying degrees by the wave orbital motions of the dominant wave. Analysis of the wavenumber response of the 9×9 boxcar filter revealed that the turbulent velocity field was contaminated by approximately 4 % of the energy of the orbital motions at the wavenumber corresponding to the dominant wave at a wind speed of 11.0 m s^{-1}. This percentage increased monotonically to 22 % as the wind speed decreased to 4.5 m s^{-1}. The reason for this increase is that as the wind speed decreases, the wavenumber of the dominant wave increases and moves closer to the cutoff wavenumber of the spatial filter. The decomposed turbulent velocities are very sensitive to contamination by the wave velocity components. In the field, the wave-induced velocities can be several orders of magnitude larger than the turbulent

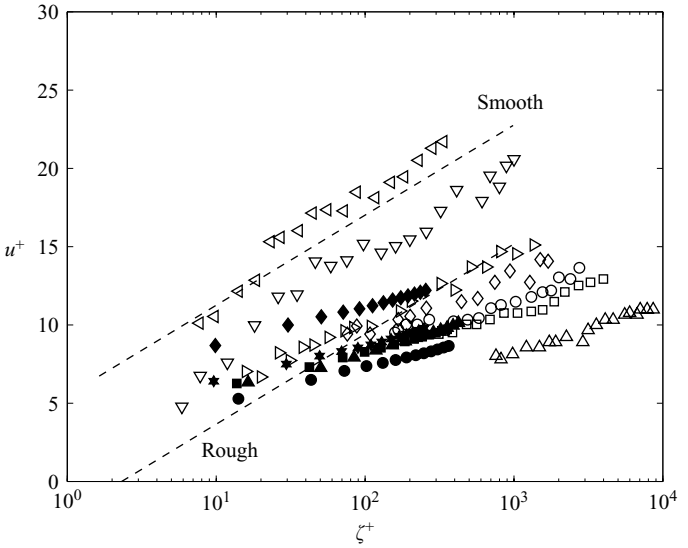

FIGURE 3. The mean streamwise velocity plotted in the form of a velocity defect law in wall coordinates. $u^+ = (U_s - U)/u_*$ and $\varsigma^+ = \varsigma u_*/\nu$. Solid symbols (present study); *, 4.5 m s^{-1}; ◆, 6.1 m s^{-1}; ●, 7.4 m s^{-1}; ■, 8.5 m s^{-1}; ▲, 11 m s^{-1}. Open symbols (CS, figure 1); ◁, 1.5 m s^{-1}; ▽, 2.6 m s^{-1}; ▷ 3.2 m s^{-1}; ◇, 4.7 m s^{-1}; ○, 6.7 m s^{-1}; □, 9.9 m s^{-1}; △, 13.1 m s^{-1}. For the present study, ζ is the distance below the surface in a wave-following coordinate system and for CS it is the distance below the mean water level. The friction velocity was estimated by computing the Reynolds stress from the decomposed turbulent velocity field and then extrapolating it to the water surface. Note, that this method produces friction velocities that are overestimated by a large margin (see § 4.3.1) and as a result these velocity profiles are biased, i.e. they are shifted downwards and to the right.

velocities. In a laboratory wind wave tank, the difference is not as great, but wave-induced velocities will still be up to an order of magnitude larger than the turbulent velocities. Therefore, the leakage of even a small percentage of the wave velocity component produces large distortions in the turbulent velocity, that is, turbulent velocities will be significantly overestimated. These errors will then be magnified when computing such quantities as turbulent shear stresses and turbulent kinetic energy.

CS computed the turbulent shear stress from turbulent velocities that were separated from the wave velocity components using a linear filtration method. Then, because their measurements were restricted to the region below the wave troughs, they linearly extrapolated the turbulent shear stress to the mean water level, and used this value to estimate the friction velocity. They found that mean velocity profiles plotted in wall coordinates (i.e. $u^+ = (U_s - U)/u_*$ versus $y^+ = u_* z/\nu$) had slopes smaller than the classical wall-layer slope of 2.5 (i.e. $1/\kappa$). They argued that these deviations in the slope were due to the influence of waves on the mean flow.

In order to compare directly with the results of CS, we estimated friction velocities in the same manner. That is, values of the turbulent shear stresses were computed from the filtered turbulent velocities. The value of the turbulent shear stress at the surface was obtained by extrapolation and this value was then used to compute the friction velocity. These estimates of u_* varied from 0.77 to 1.31 cm s^{-1} as the wind speed increased from 4.5 to 11 m s^{-1}. We will demonstrate in § 4.3.2 that this method overestimates u_* by a factor of two or more. In figure 3, the mean velocity profiles are plotted in wall coordinates using the friction velocities computed from the

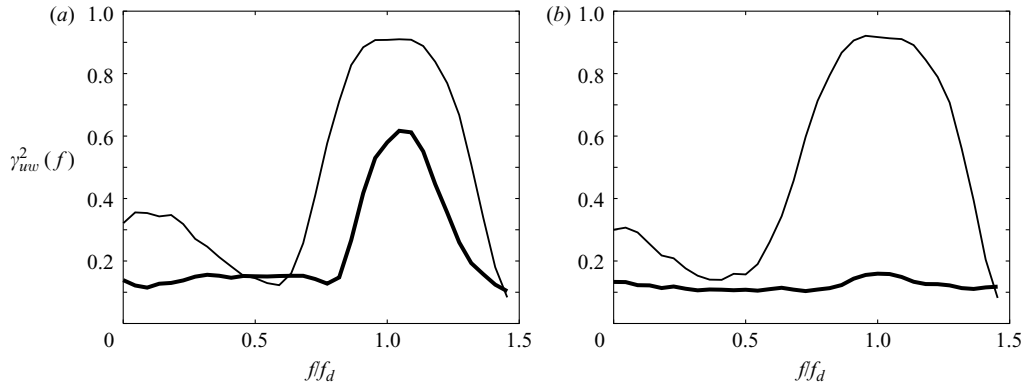

FIGURE 4. Coherence spectra of the wave and turbulent velocities at a wind speed of 4.5 m s^{-1} at (*a*) 1 mm, (*b*) 11 mm from the water surface. The frequency f is normalized by the frequency of the dominant wave f_d. Thin line, $\gamma^2_{\tilde{u}\tilde{w}}$; thick line, $\gamma^2_{u'w'}$. The coherence spectra were computed by averaging over 10 min of data.

turbulent shear stresses. Also shown plotted are the smooth and rough-wall equations for turbulent flow over a solid wall (Schlichting & Gersten 2000). The mean velocity profiles from CS (their figure 1) are also plotted in the figure for comparison. What is most noteworthy about this figure is the similarity between the two sets of velocity profiles. Both sets of profiles have very similar slopes and in both cases, almost all of the data points lie below the equation for a rough solid wall, which would indicate that these flows were in the fully rough regime.

CS argued that their velocity profiles had slopes <2.5 when wave, induced velocities were dominant compared to turbulence, and they concluded that this was evidence that the waves were influencing the mean flow. However, the errors associated with any velocity decomposition scheme will tend to be largest when the wave-induced velocities are large compared to the turbulent velocities. An equally plausible explanation for the lower slopes is that their values of u_* were significantly overestimated. This would decrease the slopes and shift the velocity profiles downward and to the right in figure 3. At their two lower wind speeds, i.e. 1.5 and 2.6 m s^{-1}, the slopes of the velocity profiles were $\sim$2.5 and the data fall in the smooth and transition regimes. At these very low wind speeds, the waves would be non-existent or of extremely small amplitude and, therefore, the wave-induced velocities were probably negligible in these two cases (Kahma & Donelan 1988). As a result, there would have been very little contamination of the turbulent velocities by the wave-induced velocities and therefore, the friction velocities at these two wind speeds are probably CS's most accurate estimates of u_*.

To explore this issue in greater depth, we examined the coherence between the velocity components. Evidence of leakage of the wave velocity components into the turbulent velocities can be obtained by computing the coherence between the streamwise and vertical components of the wave and turbulent velocity fields. The coherence between the streamwise and vertical components of the wave, $\gamma^2_{\tilde{u}\tilde{w}}$, and turbulent velocities, $\gamma^2_{u'w'}$, at a wind speed of 4.5 m s^1 at depths of 1 mm and 11 mm are shown plotted in figure 4. The corresponding frequency spectra are plotted in figure 5. In these figures, the non-dimensional frequency f/f_d is plotted on the abscissa where f_d is the dominant wave frequency. In figure 4, the magnitude of the coherence between the streamwise and vertical wave velocity components is $\sim$0.9 at frequencies

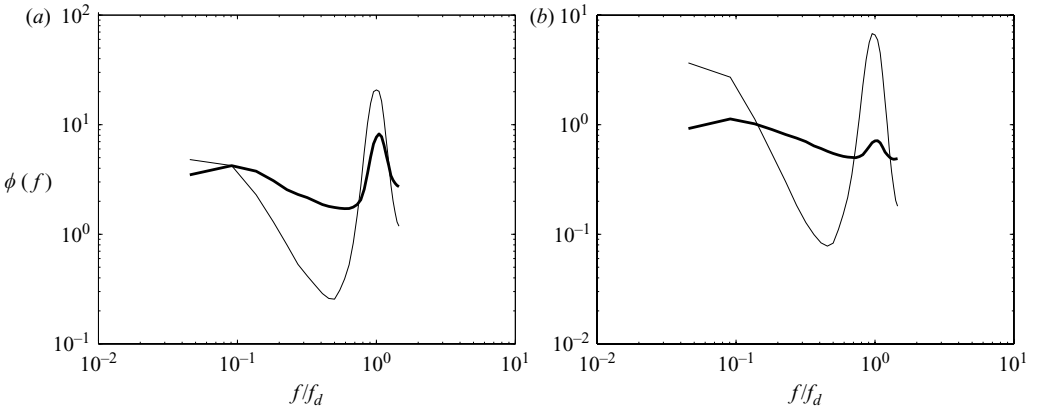

FIGURE 5. Frequency spectra of the streamwise wave and turbulent velocities at a wind speed of $4.5\,\mathrm{m\,s^{-1}}$ at (*a*) 1 mm, (*b*) 11 mm from the water surface. The frequency f is normalized by the frequency of the dominant wave f_d. Thin line, streamwise wave velocity; thick line, streamwise turbulent velocity. The frequency spectra were computed by averaging over 10 min of data.

close to the dominant wave frequency. Coherence close to one is expected because beneath water waves, the vertical and horizontal wave induced velocities should be closely correlated.

In a turbulent shear flow, the magnitude of the coherence spectrum is expected to be much less than one. In figure 4, the coherence between the two turbulent velocity components is ~0.1 at all frequencies except in figure 4(*a*) where it increases to ~0.6 at frequencies close to the dominant wave. In figure 4(*b*) the coherence spectrum computed at a depth of 11 mm has a very small peak ($\gamma^2_{u'w'} \approx 0.15$) at the dominant wave frequency indicating that there is no significant coherence between the two components of the turbulent velocity at this depth. In figure 5(*a*), plots of the frequency spectra of the turbulent and wave velocity components at the two depths are compared. As expected, at both depths, the frequency spectra of wave velocity components have large peaks centred at the dominant wave frequency. At a depth of 1 mm, the spectra of the turbulent velocity components also have large peaks centred at the dominant wave frequency. At a depth of 11 mm there are still peaks in the spectra of the turbulent velocities, but they are much smaller in amplitude. The high values of the coherence in figure 4(*a*) and the peaks in the frequency spectra in figure 5 are due to leakage of the wave velocity components into the turbulent velocity data, as described previously.

Jiang *et al.* (1990) used plots of the coherence function, similar to those plotted in figure 4, to argue that their wave–turbulence separation technique was accurate. They computed the coherence at a depth of 8.72 mm below the mean water level and at a wind speed of $4.5\,\mathrm{m\,s^{-1}}$ and found on average that $\gamma^2_{u'w'} \approx 0.2$. This led them to conclude that their wave–turbulence separation technique was accurate. However, they also presented plots of frequency spectra of the streamwise and vertical components of the turbulent velocity field at the same depth and there were prominent peaks at the dominant wave frequency. The coherence spectrum of the turbulent velocities plotted in figure 4(*b*) was computed at approximately the same depth below the mean water level as Jiang *et al.*'s (1990) coherence spectrum and the magnitudes of $\gamma^2_{u'w'}$ at the dominant wave frequency were comparable. In addition, similarly to Jiang *et al.*

(1990), we observed a peak in the frequency spectra of the turbulent velocities at the dominant wave frequency at this depth (see figure 5*b*). The amplitude of this spectral peak was approximately a factor of 10 smaller than the spectral peak observed at a depth of 1 mm. This is consistent with the reduction in the wave orbital velocities predicted using linear wave theory. Jiang *et al.* (1990) analysed the Cheung & Street (1988) data set using a nonlinear streamfunction to separate the turbulent and wave velocity components, and obtained turbulent shear stresses that agreed with Cheung & Street (1988). This suggests that there were also significant errors associated with the wave turbulence decomposition scheme employed by Jiang *et al.* (1990).

This analysis demonstrates that below the wave troughs where the magnitudes of the wave-induced velocities are relatively small, the degree to which the turbulent velocity field is contaminated by wave velocities also tends to be small. As a result, the magnitude of the coherence between the turbulent velocity components is not affected significantly by this contamination. However, above the wave trough the magnitudes of the wave-induced velocities are significantly larger. Consequently, the coherence between the turbulent velocity components at the dominant wave frequency is increased dramatically because of the contamination by the wave velocities. Therefore, we concluded that when the magnitude of the coherence (between the turbulent velocity components) is much less than one below the wave troughs, it does not necessarily follow that the wave and turbulent velocity components have been decomposed accurately. Using a spatial filter to separate the turbulent and wave velocity components gives results that are consistent with those found by CS and Jiang *et al.* (1990) using two different separation techniques. From this comparison, we concluded that these two separation techniques, and our spatial filtration method, produced turbulent velocities that were contaminated to a significant degree by the wave velocities, particularly in the crest–trough region. These contaminated turbulent velocities should not be used to compute the turbulent kinetic energy or turbulent shear stresses because the resulting errors will be magnified.

Sullivan *et al.* (2004) carried out direct numerical simulations that included a stochastic model of the effects of wave breaking on the oceanic boundary layer. They found that the slopes of the mean velocity profiles were constant and equal to 2.5. This supports our assertion that CS overestimated the values of the friction velocity and that this lead them to conclude that the flows in the aqueous boundary layer were rougher than they actually were and that the slopes of the velocity profiles were less than 2.5. As a result, we concluded that the non-dimensional velocity profiles presented in figure 3 are inaccurate. That is, they have slopes less than 2.5 and are shifted downwards and to the right because of errors in the estimated friction velocities.

4.3.2. *Velocity defect law*

The mean streamwise velocity distribution in the logarithmic layer of a neutral aqueous boundary layer can be written as,

$$\frac{U_s - U(\zeta)}{u_*} = \frac{1}{\kappa} \ln\left(\frac{\zeta}{z_o}\right), \tag{4}$$

where, U_s is the surface velocity, $U(\zeta)$ is the mean streamwise velocity, u_* is the friction velocity on the waterside, z_o is the roughness length, ζ is the vertical distance below the water surface in the wave-following coordinate system, and κ is the Kármán constant and its value is taken as 0.4 (Wu 1975). As was discussed earlier in § 4.3, the mean velocity profiles were found to be logarithmic, and therefore (4) is an accurate representation of the mean streamwise flow.

In addition to the method employed by CS, several other methods for estimating the waterside friction velocity are reported in the literature. For example, Wu (1975) computed u_* from a linear fit to the logarithmic mean velocity profiles measured below the wave troughs. Thais & Magnaudet (1996) estimated u_* by assuming that the shear stress in the water was equal to the shear stress measured in the air. Assuming that the shear stress in the water is equal to the air-side value, as Thais & Magnaudet (1996) did, is equivalent to assuming that there is no partitioning of the stress into tangential and wave components. Banner & Peirson's (1998) measurements and Makin & Kudryavtsev's (2002) model predictions show that, for the very young waves present in wind wave tanks, this assumption may lead to significant overestimation of the water-side tangential stress.

Based on this information, we decided to adopt an approach similar to Wu (1975) and obtain estimates of u_* and z_o values by fitting (4) to the measured velocity profiles. The mean velocity, $U(\zeta)$ and the surface velocity, U_s, were measured as described above, leaving two unknowns in equation (4), u_* and z_o. The values of u_* and z_o were obtained at each wind speed by performing a least-squares regression of the data to (4). The average value of the correlation coefficient was 0.99, confirming that the mean velocity profiles were logarithmic and that (4) was an accurate description of the mean streamwise flow in the aqueous boundary layer. The values of u_* were obtained from the slope of the fitted line, and the value of z_o was computed using U_s and the intercept. The values of z_o range from 0.12×10^{-3} to 3.4×10^{-3} mm and are given in table 2. The thickness of the viscous sublayer, $\delta_v = 5\upsilon/u_*$, varied from 1.3 mm to 0.63 mm as the wind speed increased from 4.5 m s^{-1} to 11 m s^{-1}, see table 2 ($\nu = 8 \times 10^{-7}$ m^2 s^{-1}). Clearly, $\delta_v \gg z_o$, and therefore, the flow in the aqueous boundary layer at all wind speeds was hydrodynamically smooth. The values of u_* (see table 2) varied from 0.32 to 0.63 m s^{-1} as the wind speed increased. These estimates are approximately a factor of two smaller than the values computed from the turbulent shear stresses in § 4.3.1.

The mean streamwise velocity profiles at the five wind speeds are plotted in the form of a velocity defect law in wall coordinates, in figure 6. Also plotted in figure 6 is a line representing the law of the wall for a turbulent flow with a zero pressure gradient over a smooth wall (Schlichting & Gersten 2000). The plot shows that, at all wind speeds, the flow is hydrodynamically smooth. The similarities of the wind drift layer to a boundary layer over a solid wall will be discussed further in § 4.5.

The fact that (4) fits the mean streamwise velocity profiles so well (i.e. average correlation coefficient of 0.99) confirms that even though there was a large air–water temperature difference, the flow in the upper 2.5 cm of the water was not significantly affected by thermal stratification. This follows because if the buoyant production of turbulence was important, the velocity profiles would not have been logarithmic and it would have been necessary to fit them with a log–linear type of equation (Turner 1973). Thus, we concluded that the near-surface turbulence was predominantly mechanically driven and did not appear to be significantly influenced by buoyant convection (Kundu & Cohen 2002).

4.4. *Energy dissipation*

Estimates of the rate of energy dissipation, ε, beneath wind waves provide information about the availability of energy within the water column for generating currents and increasing the transport of gas and heat across the air–water interface (Melville 1994). Doron *et al.* (2001) compared five different methods of estimating the energy dissipation and showed that the 'direct' method that uses velocity gradients computed

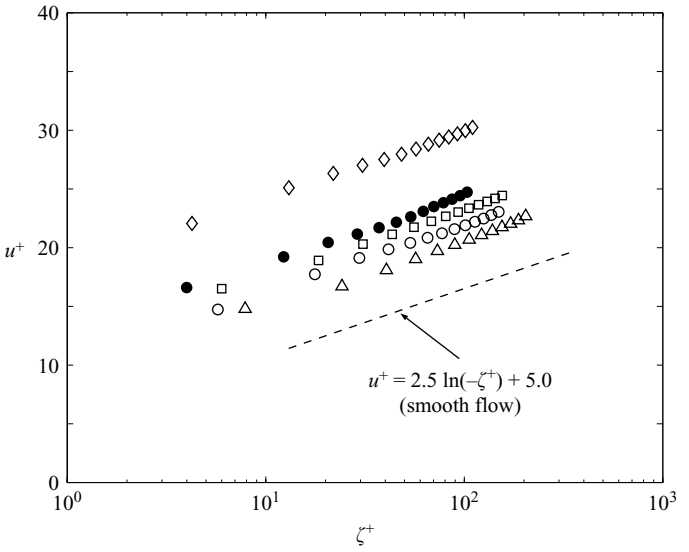

FIGURE 6. The mean streamwise velocity plotted in the form of a velocity defect law in wall coordinates. $u^+ = (U_s - U)/u_*$ and $\varsigma^+ = \varsigma u_*/\nu$. ●, 4.5 m s^{-1}; ◇, 6.1 m s^{-1}; ○, 7.4 m s^{-1}; □, 8.5 m s^{-1}; △, 11.0 m s^{-1}. The friction velocities were computed by fitting equation (4) to the mean velocity profiles presented in figure 2. This method produces accurate estimates of u_* and therefore, these velocity profiles are accurate, i.e. unbiased.

from the two-dimensional turbulent velocity field obtained from DPIV measurements was the most accurate. In § 4.3.1, it was shown that the decomposed turbulent velocity components were contaminated by the wave component. Here we will demonstrate that the effect of this contamination on the turbulent velocity gradients is small and therefore, reasonable estimates of ε can be obtained using the direct method.

In order for this to be true, the turbulent velocity gradients must be considerably larger than the wave-induced velocity gradients. The average magnitude (averaged in both space and time) of the velocity gradients of the wave and turbulent velocity components were computed at different wind speeds within the top 1 cm layer (i.e. the region of largest velocity gradients). It was observed that the turbulent velocity gradients were on average approximately 2.5 times larger than the wave-induced velocity gradients at all wind speeds. The worst contamination occurred at the lowest wind speed when 22 % of the dominant wave velocities were not filtered out of the turbulent velocity data. At this wind speed, the turbulent velocity gradients are 2.8 times larger than the wave velocity gradients. An estimate of the resulting relative error in the turbulent velocity gradients can be obtained simply by dividing 22 % by 2.8, which gives 7.9 %. At the highest wind speed, this relative error is reduced to 1.5 %. This simple analysis indicates that the filtered turbulent velocity components can be used to compute accurate estimates of ε.

The rate of energy dissipation, ε, can be computed using the 'direct' method with the following equation,

$$\varepsilon = 3\nu \left\{ \overline{\left(\frac{\partial u'}{\partial x}\right)^2} + \overline{\left(\frac{\partial w'}{\partial z}\right)^2} + \overline{\left(\frac{\partial u'}{\partial z}\right)^2} + \overline{\left(\frac{\partial w'}{\partial x}\right)^2} + 2\overline{\left(\frac{\partial u'}{\partial z}\frac{\partial w'}{\partial x}\right)} + \frac{2}{3}\overline{\left(\frac{\partial u'}{\partial x}\frac{\partial w'}{\partial z}\right)} \right\}. \tag{5}$$

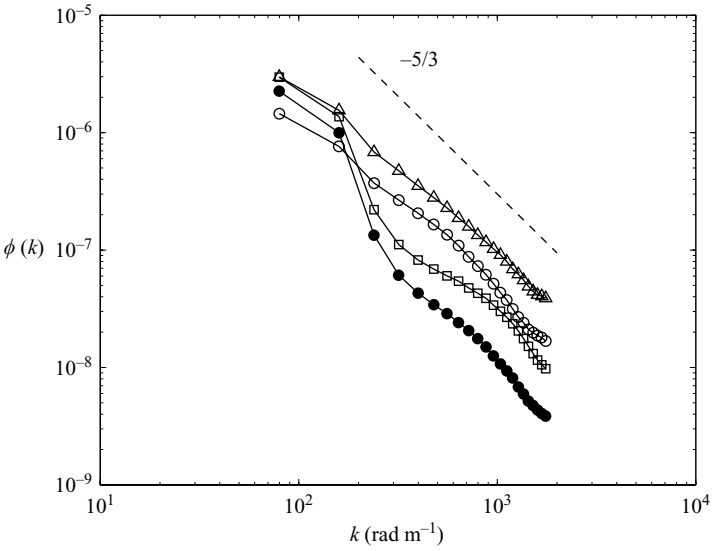

FIGURE 7. Wavenumber spectra of the instantaneous velocity at a depth of 1 mm from the surface. △, streamwise velocity at 11.0 m s^{-1}; □, streamwise velocity at 4.5 m s^{-1}; ○, vertical velocity at 11.0 m s^{-1}; ●, vertical velocity at 4.5 m s^{-1}. The spectra were computed by averaging over 10 min of data at a given depth.

where, the overbar denotes time-averaged values (Doron *et al.* 2001). To provide further evidence that the direct method is accurate when applied to our decomposed turbulent velocity data, estimates of ε computed using the direct method were compared to values estimated by fitting a line to the wavenumber spectrum of the streamwise velocity within the inertial subrange. The rate of energy dissipation within the inertial subrange is given by,

$$\Phi_u(k) = \frac{18}{55}\left(\frac{8}{9\alpha}\right)\varepsilon^{2/3}k^{-5/3} \tag{6}$$

where, Φ_u is the wavenumber spectrum of the streamwise velocity, k is the wavenumber within the inertial subrange and α is a constant equal to 0.4 (Hinze 1975; Veron & Melville 1999). The wavenumber spectra of the streamwise and vertical velocities were computed at all depths and, averaged over 10 min. The wavenumber spectra at a depth of 1 mm are shown plotted in figure 7, for the lowest and highest wind speeds. A well-defined inertial subrange was observed over a relatively large range of wavenumbers in both wavenumber spectra at the highest wind speed. However, at the lowest wind speeds, the inertial subrange was manifested only in the higher wavenumber range. At depths greater than 11 mm from the surface, the inertial subrange was not always present in the spectra of the streamwise velocity. Therefore, estimates of ε were computed only at depths from 1 to 11 mm using (6). The values of ε computed using the linear fit and the direct method and averaged over 11 mm depth are compared in table 3. These two methods give independent estimates of ε. A comparison of the results in table 3 indicates that the values of ε estimated using the line fit method are on average 44 % larger than the values estimated using the direct method. This is comparable to the results of Doron *et al.* (2001) who found that estimates of ε made using (6) were 53 % larger than those obtained using the direct method. This comparison and the previous analysis both confirm that the estimates

	Rate of energy dissipation ε ($cm^2\,s^{-3}$)	
U_∞($m\,s^{-1}$)	Linear fit	Direct
4.5	1.39	1.13
6.1	2.17	1.66
7.4	3.69	2.43
8.5	4.19	2.69
11.0	6.30	3.95

TABLE 3. Values of ε computed using the linear-fit and the direct methods at various wind speeds, U_∞. The values are averaged over a depth of 11 mm.

of ε calculated from the decomposed turbulent velocity gradients using the direct method are acceptable and therefore, the direct method was used in all subsequent analyses.

Another issue to consider is whether the DPIV measurements had sufficient spatial resolution to resolve the shear responsible for the dissipation of the turbulent kinetic energy. The smallest spatial scale that was resolved by the DPIV was 3.5 mm, corresponding to a wavenumber, $k = 1800\,rad\,m^{-1}$, and the Kolmogorov length scale, η, ranged from 150 to 320 μm. These values give a range of $k\eta$ from 0.27 to 0.57. In order to obtain reliable estimates of ε, it is not necessary to resolve the Kolmogorov length scale. Tennekes & Lumley (1972) have shown that almost the entire dissipation takes place for $k\eta < 5$ and that the maximum dissipation occurs at $k\eta = 0.2$. Based on the dissipation spectrum shown in Tennekes & Lumley (1972), we estimated that our calculated values of ε captured 60 % to 90 % of the total dissipation with an average value of 75 %. Ideally, this value should exceed 90 %, but given that the uncertainty in the values of ε computed by two methods was found to be 44 %, we concluded that the spatial resolution of the DPIV measurements was sufficient.

The vertical profiles of ε at five wind speeds are plotted in figure 8. The profiles show that ε was enhanced significantly near the surface and that ε did not vary significantly below a depth of ~1.5 cm. As the wind speed increased from 4.5 to 11 $m\,s^{-1}$, the rate of dissipation at all depths increased by a factor of approximately 3.5. A regression analysis of the ε profiles showed that, in the top 1.5 cm layer at all wind speeds, ε was proportional to $\zeta^{-0.5}$.

In a wall-layer or constant stress layer, ε scales with z, the distance from the wall and the friction velocity, u_*, as follows,

$$\varepsilon = \frac{u_*^3}{\kappa z}, \tag{7}$$

where $\kappa = 0.4$ is the Kármán constant. Soloviev, Vershinsky & Bezverchinii (1988) hypothesized that in the upper ocean, ε should scale with the depth, z, the friction velocity, u_*, and the acceleration due to gravity, g. Using dimensional analysis they found that $(\varepsilon z/u_*^3)$ should be a function solely of (gz/u_*^2). In figure 9, the normalized rate of energy dissipation $(\varepsilon\kappa\zeta/u_*^3)$ is plotted versus $(g\varsigma/u_*^2)$, where ζ is the depth from the fluctuating free surface. Using this scaling, the normalized rate of energy dissipation $(\varepsilon\kappa\zeta/u_*^3)$ for a constant stress layer would be unity at all depths (Agrawal *et al.* 1992). The data in figure 9 collapse into a relatively narrow band indicating that the scaling proposed by Soloviev *et al.* (1988) applies beneath small-scale wind waves. The values of normalized dissipation at a depth of 1 mm were in the range of one

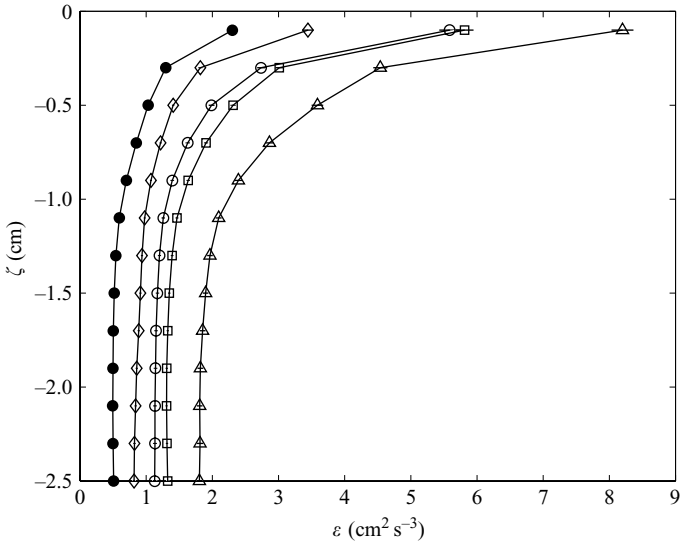

FIGURE 8. Vertical profiles of the rate of energy dissipation, ε. The error bars indicate the standard error of the mean. The values of ε at a given depth in both plots are time-averaged over 10 min and spatially averaged over the width of the PIV field of view. ●, 4.5 m s^{-1}; ◇, 6.1 m s^{-1}; ○, 7.4 m s^{-1}; □, 8.5 m s^{-1}; △, 11.0 m s^{-1}.

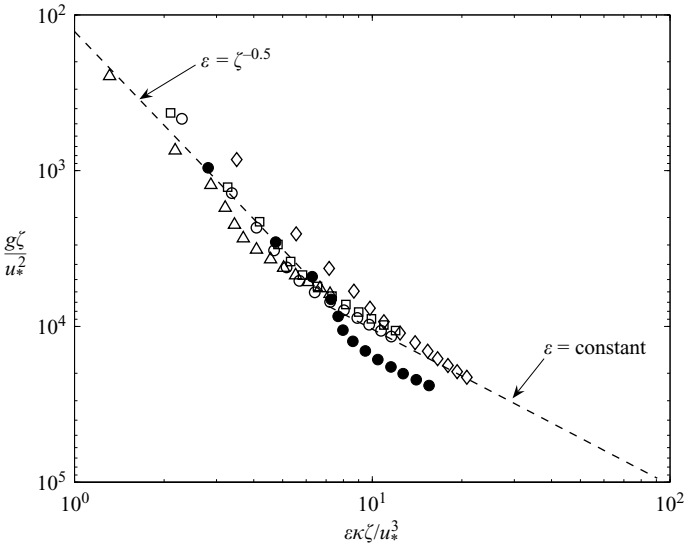

FIGURE 9. Plot of the rate of energy dissipation, ε, versus the depth, ζ, normalized in wall coordinates. ●, 4.5 m s^{-1}; ◇, 6.1 m s^{-1}; ○, 7.4 m s^{-1}; □, 8.5 m s^{-1}; △, 11.0 m s^{-1}.

to three, slightly larger than the value predicted for a wall layer ($\varepsilon\kappa z/u_*^3 = 1$). At a depth of 25 mm values of the normalized dissipation ranged from 7 to 20, indicating that the dissipation was enhanced by approximately one order of magnitude, relative to the wall layer at this depth. The plot shows that for $g\varsigma/u_*^2$ less than approximately 10^4, $\varepsilon \propto \zeta^{-0.5}$ and that at greater depths, ε is approximately constant.

The Kolmogorov time and length scales were computed from ε. It was found that the Kolmogorov length scale, η, decreased as the wind speed increased. Immediately beneath the water surface at a depth of 1 mm, η decreased from 220 μm to 160 μm as the wind speed increased from 4.5 m s^{-1} to 11.0 m s^{-1}. Furthermore, η increased by approximately a factor of 1.5 from a depth of 1 mm to 25 mm. The Kolmogorov time scale, τ, behaved similarly, that is, τ decreased with increasing wind speed. At a depth of 1 mm, τ decreased from 60 ms to 30 ms as the wind speed increased from 4.5 to 11.0 m s^{-1}. Also, τ increased by a factor of approximately 2 from a depth of 1 mm to 25 mm at all wind speeds. Thais & Magnaudet (1996) found that $\tau = 60$ ms at a wind speed of 6.0 m s^{-1} which is comparable to the values from this study.

4.5. *Discussion: wind drift layer*

The mean velocity profiles were plotted in the form of a velocity defect law in figure 6. The profiles at all five wind speeds lie above the line for the equation for hydrodynamically smooth flow over a solid wall. This equation is referred to as the universal velocity-distribution law for a smooth wall since velocity profiles measured above hydrodynamically smooth solid-walls tend to collapse onto this curve (Schlichting & Gersten 2000). Hsu *et al.* (1981) argued that in the wave-following coordinate system, the mean velocity profiles tend to follow the waveform and the water waves are not regarded as surface roughness. Therefore, the roughness length computed from these mean velocity profiles may only account for small ripples (i.e. capillary waves in the present case), and hence, the flows were hydrodynamically smooth. The fact that the velocity profiles lie above the smooth-wall equation indicates that the frictional drag is actually less than would be present on a smooth wall. In general, the presence of roughness elements increases the frictional drag, but in some cases a moderately rough surface reduces drag (Jiménez 2004). For example, Sirovich & Karlsson (1997) showed that a random distribution of protrusions reduced the drag by >10 % compared to a smooth wall. In the case of the aqueous boundary layer beneath short wind waves the roughness elements are comprised of three-dimensional waves and ripples and their location on the surface is quite random. Therefore, it is possible that these roughness elements reduce the drag in the aqueous boundary layer to a value that is smaller than that over a smooth wall.

Another noteworthy feature of this velocity defect plot is that not all the profiles are monotonic with wind speed. That is, one would expect the profile at the highest wind speed to be the lowest curve and as wind speed decreases the curves to plot progressively higher. In figure 6, the profiles are positioned vertically as follows 11, 7.4, 8.5, 4.5 and 6.1 m s^{-1} from lowest to highest. This behaviour is probably due to uncertainty in the estimated values of U_S and u_*. In table 2, the uncertainty in U_s and u_* were estimated as ± 10 % and ± 20 %, respectively. This level of uncertainty can explain the non-monotonic behaviour of the velocity profiles in figure 6.

There is considerable uncertainty in the literature regarding the properties of the aqueous boundary layer. CS made laboratory measurements at a fetch of 13 m and concluded that at wind speeds as low as 3.2 m s^{-1} the flow in the aqueous boundary layer was hydrodynamically rough. Wu (1975) conducted laboratory measurements at a fetch of 11 m and at wind speeds from 1 m s^{-1} to 7 m s^{-1} and concluded that the flow was hydrodynamically smooth. Lin & Gad-el-Hak (1984) found that at a wind speed of 10 m s^{-1} and fetches varying from 2 m to 5 m, the aqueous boundary layer was in the transition regime. In this study, we found that the flow was always hydrodynamically smooth within the given range of wind speeds. Some of these seemingly contradictory

results are almost certainly due to errors incurred when estimating z_o. For example, even an error as small as 5 % in the value of U_s may produce an error of ~200 % in z_o.

In § 4.3.1, evidence was presented that showed that CS had significantly overestimated u_*. As was discussed, this would make the aqueous boundary layer appear rougher than it actually was since it shifts the velocity profiles downwards and to the right in plots such as figure 3. In addition, in § 4.3.1 it was argued that at the two lowest wind speeds the estimated friction velocities were more accurate and in these cases the boundary layer was found to be smooth or in transition. Therefore, it is possible that the aqueous boundary-layer flows in CS were not hydrodynamically rough, but were actually in the transition or smooth regime. If this is correct, then the results from previous laboratory studies are consistent with the findings of this study because in all cases the flow in the aqueous boundary layer was found to be either smooth or in the transition regime. Bourassa (2000) reanalysed the field data of Bye (1965) and Churchill & Csanady (1983) and found that the flow in the wind drift layer could be in any of the three regimes; smooth, transition or rough. However, 8 of the 10 cases he reanalysed (see table 1 in Bourassa 2000) were found to be hydrodynamically rough. These results suggest that at short fetches in laboratory wind wave tanks, the aqueous boundary layer is smooth or in the transition regime and that in the field, at longer fetches, the flow tends to be hydrodynamically rough. Additional experiments either in the field or at longer fetches in the laboratory will be required to resolve this issue with certainty.

It is important to recall that the only feature that the velocity profiles measured in this study and previous laboratory or field studies have in common with each other and with wall-bounded shear flows is that in all cases a logarithmic velocity profile was observed. This similarity may not be particularly important since the presence of a logarithmic layer near a solid surface or near an air–water interface can be justified solely using dimensional arguments (Kundu & Cohen 2002). That is, a logarithmic velocity distribution is derived if it is argued that the mean velocity gradient depends only on the distance from the surface and on the relevant velocity scale, which is traditionally taken to be the friction velocity. Therefore, the presence of a logarithmic profile does not necessarily mean that the flow in the aqueous boundary layer is completely analogous to a wall-bounded shear flow.

Thais & Magnaudet (1996) reported that below the wave troughs of laboratory-generated wind waves, ε was enhanced relative to a wall layer by up to a factor of approximately three. Figure 9 shows that in this study, ε was enhanced relative to a wall layer by a factor of approximately 10 at a depth of 25 mm. Given the uncertainties in the estimates of ε and u_*, these results can be considered comparable. In the upper ocean, values of ε have been observed that were several orders of magnitude larger when compared to an equivalent wall layer (Kitaigorodskii *et al.* 1983; Agrawal *et al.* 1992).

It is of interest to compare the magnitudes of ε observed in this study with previous laboratory and field measurements. Thais & Magnaudet (1996) measured values of ε as high as approximately $7\,\mathrm{cm^2\,s^{-3}}$ below the troughs of laboratory wind waves at a fetch of 26 m. Kitaigorodskii *et al.* (1983) and Terray *et al.* (1996) conducted field experiments and reported values of ε in the range of 1 to $5\,\mathrm{cm^2\,s^{-3}}$ within the top metre. Melville, Veron & White (2002) measured ε beneath mechanically generated plunging breaking waves and reported values ranging from 0.002 to $0.05\,\mathrm{cm^2\,s^{-3}}$. They were only able to make measurements starting three wave periods after the breaking event, which accounts for these low values. Extrapolating their results back in time closer to the onset of breaking, gives a value of ε of order $1\,\mathrm{cm^2\,s^{-3}}$. In this

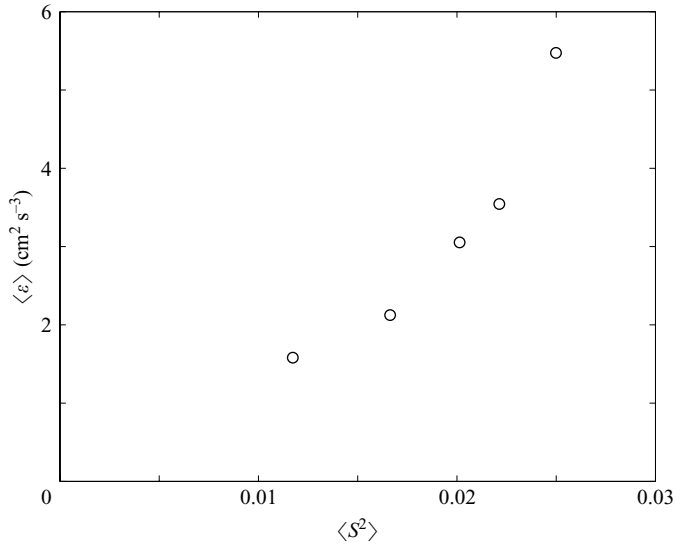

FIGURE 10. Plot of the mean square wave slope, $\langle S^2 \rangle$, versus the rate of energy dissipation, $\langle \varepsilon \rangle$, (averaged over top 1 cm layer) at wind speeds of 4.5 m s^{-1}, 6.1 m s^{-1}, 7.4 m s^{-1}, 8.5 m s^{-1}, and 11.0 m s^{-1}. Both quantities are time-averaged over 10 min and spatially-averaged over the width of the PIV field of view.

study, values of ε in the range 0.5 to 8 cm^2 s^{-3} were observed (see figure 8) which are comparable with both the field and laboratory results cited above.

One common feature observed in both field and laboratory studies is that the values of ε are enhanced relative to the wall-layer estimates. This indicates that the physical mechanism(s) of turbulence production and dissipation beneath wind-sheared air–water interfaces is different from that adjacent to a solid wall. In both cases, turbulence is produced via shear production, but beneath the wind-driven interface, turbulence is also produced by wave breaking and possibly via wave–turbulence interactions (Thais & Magnaudet 1996). Thais & Magnaudet (1996) argued that a dimensionless parameter, $R^2 = (a\omega/u_*)^2$, which is the square of the ratio between the wave orbital velocity at the surface and the friction velocity, is an indicator of the strength of wave–turbulence interactions. They hypothesized that significant wave-turbulence interactions will occur when R^2 is of the order of 200 and that these interactions will produce turbulence that is enhanced relative to a wall layer. In this study, values of R^2 were computed at all wind speeds and they ranged from 130 to 250. These values are of the order of 200, and if Thais & Magnaudet's (1996) hypothesis is correct, significant wave–turbulence interactions were occurring beneath the wind waves in this study.

The average values of the mean square wave slope, $\langle S^2 \rangle$, are plotted versus $\langle \varepsilon \rangle$ the rate of dissipation depth-averaged over the upper 1 cm, in figure 10. The plot shows that $\langle S^2 \rangle$ and $\langle \varepsilon \rangle$ are correlated and that there is a nonlinear relationship between them. Various workers have observed a strong correlation between the air–water gas transfer velocity and the mean-square wave slope (for example, see Jähne *et al.* 1987; Bock *et al.* 1999; Frew *et al.* 2004). Jähne *et al.* (1987) argued that this correlation was because the mean-square wave slope is a measure of the near-surface turbulence generated by waves. The correlation observed in figure 10 confirms this hypothesis

since it demonstrates that steeper waves, on average, do generate stronger near-surface turbulence.

5. Microscale breaking waves

5.1. *Detection scheme*

Siddiqui *et al.* (2001) observed that coherent structures are generated in the crests of microscale breaking waves. These coherent structures disrupt the skin layer and produce the thermal wakes that are visible in the IR images. A series of four IR images sampled at a wind speed of $7.4\,\mathrm{m\,s^{-1}}$ and the corresponding turbulent vorticity fields obtained from the DPIV data are shown in figure 11. In figure 11(*a*), the vorticity plot shows a wave crest that has travelled approximately a third of the distance across the DPIV field of view. Note that, the DPIV field of view is delineated with a thick black line in the IR images. In the corresponding IR image, no warm wake is visible (i.e. this wave did not disrupt the skin layer) and no strong coherent structures are observed in the crest region, indicating that this was a non-breaking wave. In figure 11(*b*), this non-breaking wave has advanced more than half way across the DPIV field of view and there is still no warm wake visible in the corresponding IR image. However, another wave has just crossed the upwind end of the DPIV field of view and its warm wake is visible in the IR image. This warm wake was created by a microscale breaking wave when it disrupted the cool skin layer. The leading edge of this microscale breaking wave has travelled approximately halfway across the DPIV field of view in figure 11(*c*). The leading edge of this breaker is clearly visible in the corresponding vorticity plot and coherent structures are visible in the crest of the breaker. In figure 11(*d*), the leading edge of the wake has propagated to the downwind end of the DPIV field of view, and in the corresponding vorticity plot, strong coherent structures can be observed along the entire crest region of the breaking wave. This sequence of plots provides an illustration of the signature that a typical microscale breaking wave creates in the IR images and vorticity fields. That is, microscale breaking waves generate strong persistent vortices or coherent structures in their crests that disrupt the cool skin layer and create the wakes that are visible in the IR images. Non-breaking waves do not generate coherent structures and hence do not disrupt the skin layer. Therefore, we concluded that it would be logical to develop a technique for detecting microscale breaking waves based on the statistical properties of the vorticity in the crest region.

We developed an algorithm to detect microscale breaking waves based on the variance of vorticity in the wave crest, computed from the instantaneous velocity fields. In this algorithm, the surface profile data were used to determine when a wave crest was within the DPIV field of view. A wave crest was defined as any portion of the wave that has a surface displacement greater than a quarter of the r.m.s. wave amplitude. If any portion of the wave crest was within the field of view, a region-of-interest (ROI) was defined within the corresponding velocity field. The length of the ROI was set equal to a quarter of the dominant wavelength (see table 1) and its depth to 1 cm. This depth was chosen because the size of the coherent structures generated beneath microscale breaking waves were $O(1\,\mathrm{cm})$ (Siddiqui *et al.* 2001). The ROI was centred at the location of the maximum surface displacement, η_{max}. The variance of the vorticity within the ROI was used as the criterion for detecting microscale breaking waves. The magnitude of the vorticity threshold (Ω_{max}) was selected by comparing sequences of IR images and the corresponding vorticity fields and was set equal to $70\,\mathrm{s^{-2}}$. We conducted a detailed comparison of this microscale breaking wave detection scheme

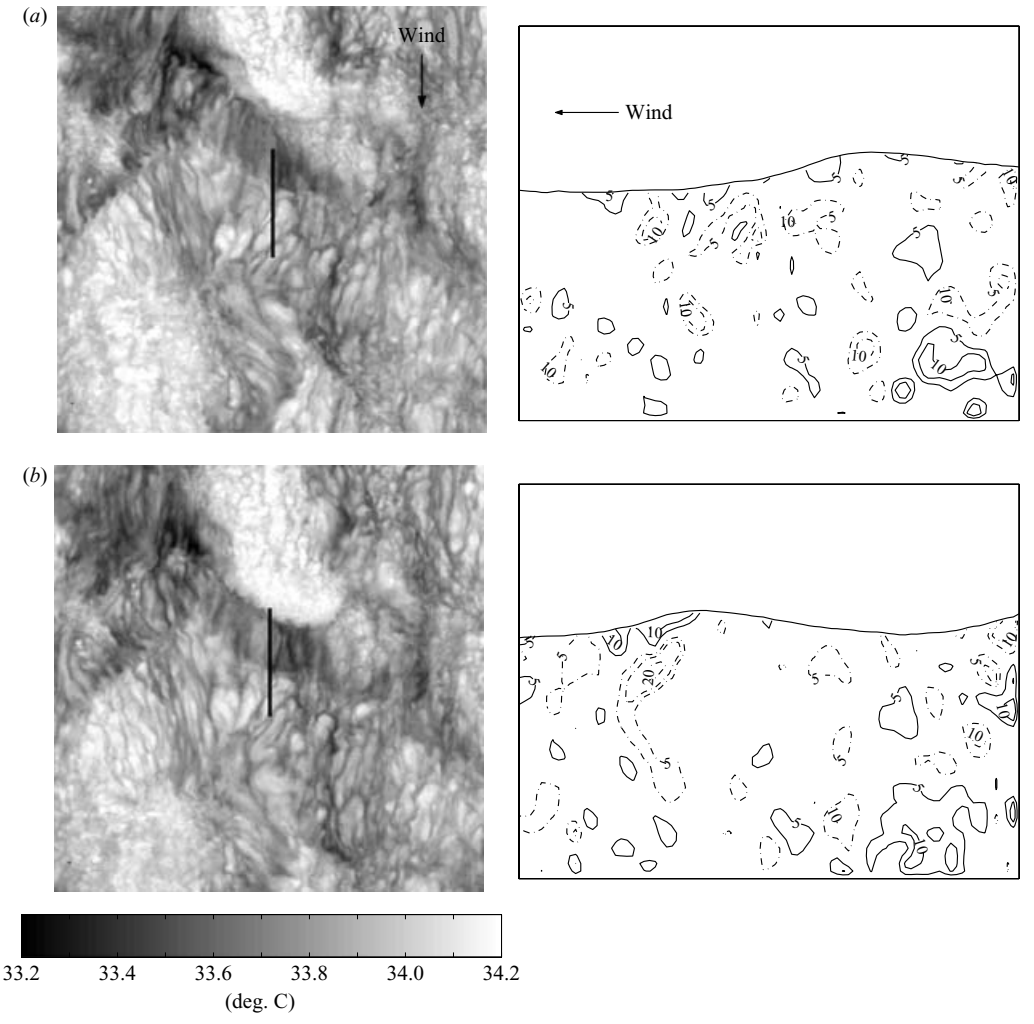

FIGURE 11(*a*, *b*). For caption see facing page

with two other schemes, one based on the areal coverage of the thermal wakes in the IR images, and the other using the wave slope as the detection parameter (Loewen & Siddiqui 2006). We found that at wind speeds lower than $7\,\mathrm{m\,s^{-1}}$, the IR and wave slope techniques significantly overestimated the number of microscale breaking waves, whereas, the present scheme accurately detects microscale breaking waves over the entire wind-speed range with an average accuracy of 92 %. See Loewen & Siddiqui (2006) for more details about the detection scheme and its validation.

All of the DPIV data, i.e. 9000 velocity fields and their corresponding surface profiles (10 min of data at 15 Hz), at each wind speed were then analysed using this detection scheme. A particular wave crest typically appeared in two to four velocity fields and the corresponding surface profiles, depending on its phase speed. The variance of the vorticity within the ROI , the wave slope on the downwind face of the wave, and the wave amplitude were computed for each field that the wave crest appeared in. The maximum values of the variance of the vorticity (Ω_{max}), wave slope (S_{max}) and amplitude (η_{max}) were computed in all fields associated with a given wave crest. If

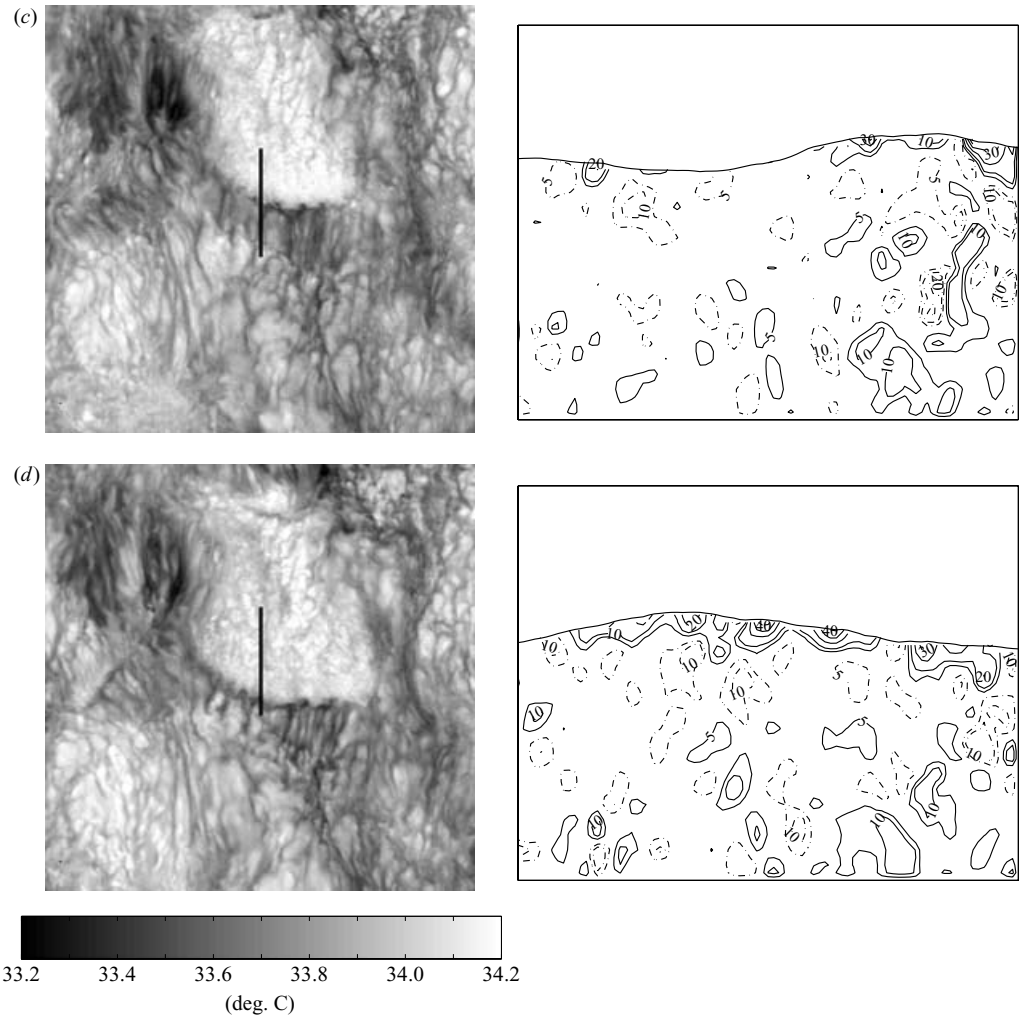

FIGURE 11. Four simultaneously sampled pairs of IR images (left-hand column) and DPIV instantaneous vorticity fields (right-hand column) at a wind speed of 7.4 $\mathrm{m\,s^{-1}}$. The sample rate for both the IR images and the DPIV fields was 15 Hz. The dimensions of the IR image are 34.3 cm $\times$ 34.3 cm and the size of the vorticity plot is 7.7 cm $\times$ 5.4 cm. The location of the DPIV field of view is marked with a vertical black line in the IR images. Solid contours correspond to counterclockwise vorticity and dash-dotted contours to clockwise vorticity.

Ω_{max} exceeded the threshold value of $70\,\mathrm{s^{-2}}$ in any field, the wave was identified as a microscale breaking wave and if $\Omega_{max} < 70\,\mathrm{s^{-2}}$, it was identified as a non-breaking wave. Note that Ω_{max}, S_{max} and η_{max} typically occurred in the same field, but not always. The velocity fields associated with breaking waves were then conditionally sampled. For each wave, the velocity field in which the maximum value of the variance of the vorticity, Ω_{max}, occurred was designated as the representative field. Conditionally sampling the velocity fields in this manner has several advantages. First, for a given wave, it identifies the velocity field in which the signature of microscale breaking is the strongest. Secondly, these velocity fields occur at approximately the same phase in the breaking process. To be consistent, non-breaking velocity fields were also conditionally sampled in the same manner. This conditional sampling selects

	$\langle S_{max} \rangle$		$\langle \eta_{max} \rangle$ (cm)	
U_∞ (m s^{-1})	Breaking	Non-breaking	Breaking	Non-breaking
4.5	0.32	0.23	0.40	0.30
6.1	0.37	0.28	0.66	0.48
7.4	0.42	0.28	0.82	0.51
8.5	0.45	0.31	0.94	0.54
11.0	0.48	0.30	1.16	0.57

TABLE 4. Values of $\langle S_{max} \rangle$, the average maximum wave slope, and $\langle \eta_{max} \rangle$, the average maximum wave amplitude for microscale breaking and non-breaking waves at wind speeds, U_∞.

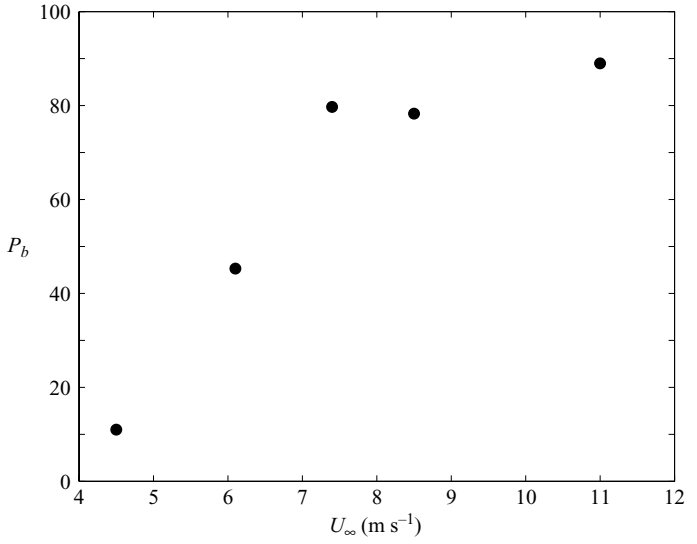

FIGURE 12. The percentage of microscale breaking waves (P_b) versus wind speed, U_∞.

a single velocity field for each wave and this allows meaningful comparisons to be made between microscale breaking waves and non-breaking waves.

5.2. *Characteristics of microscale breaking waves*

The percentage of microscale breaking waves detected using the vorticity threshold technique is plotted as a function of wind speed in figure 12. The plot shows that at a wind speed of 4.5 m s^{-1} ($U_{10} = 6.3$ m s^{-1}), the breaking percentage equalled 11 % and it increased sharply to approximately 80 % at a wind speed of 7.4 m s^{-1} ($U_{10} = 11.5$ m s^{-1}). The breaking percentage then increased to 90 % at a wind speed of 11 m s^{-1} ($U_{10} = 18.6$ m s^{-1}). The average values of the maximum wave slope on the forward face, $\langle S_{max} \rangle$, and the maximum wave amplitude, $\langle \eta_{max} \rangle$, were computed for both breaking and non-breaking waves and are presented in table 4. As the wind speed increased from 4.5 to 11.0 m s^{-1}, $\langle S_{max} \rangle$ increased from 0.32 to 0.48 and from 0.23 to 0.30 for breaking and non-breaking waves, respectively. Over the same wind speed range $\langle \eta_{max} \rangle$ increased from 0.4 to 1.16 cm and from 0.3 to 0.57 cm for breaking and non-breaking waves, respectively. These results show that microscale breaking waves were on average, 45 % steeper and 60 % larger in amplitude than non-breaking waves.

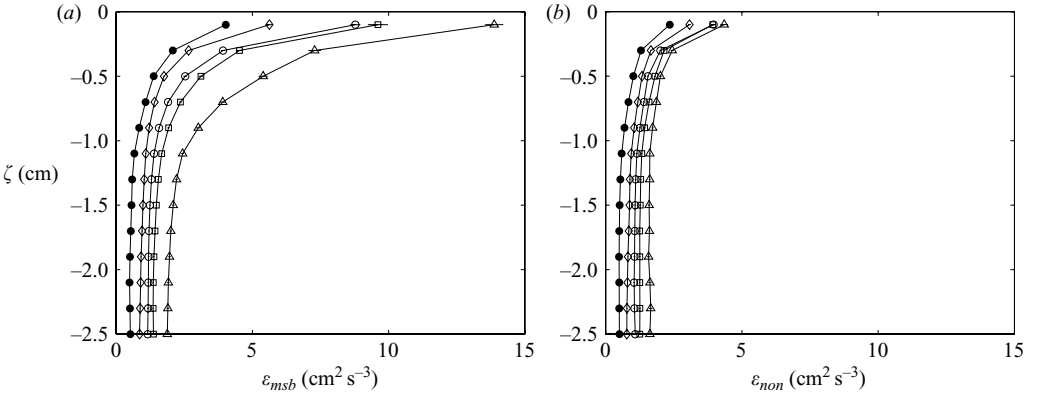

FIGURE 13. Vertical profiles of the rate of energy dissipation beneath (*a*) microscale breaking waves (ε_{msb}) and (*b*) non-breaking waves (ε_{non}). The error bars indicate the standard error of the mean. ●, 4.5 m s^{-1}; ◇, 6.1 m s^{-1}; ○, 7.4 m s^{-1}; □, = 8.5 m s^{-1}; △, 11.0 m s^{-1}. ζ is the vertical coordinate referenced to the water surface. The values of ε at a given depth in both plots are ensemble-averaged beneath (*a*) microscale breaking waves or (*b*) non-breaking waves and are spatially-averaged over the width of the PIV field of view.

Using the conditionally sampled velocity fields, the rate of turbulent kinetic energy dissipation was computed beneath breaking and non-breaking waves using the direct method. The vertical profiles of the dissipation rate beneath microscale breaking waves, ε_{msb}, and beneath non-breaking waves, ε_{non}, are shown in figure 13. The values of ε_{msb} increased by a factor of approximately 7.0 going from a depth of 15 mm to 1 mm, while the values of ε_{non} increased only by a factor of approximately 3.5. However, these plots also show that deeper in the water column, at a depth of ~25 mm, the dissipation rates beneath breaking and non-breaking waves are approximately equal at a given wind speed. At a depth of 1.0 mm, ε_{msb} was 1.7 to 3.2 times greater than ε_{non} at wind speeds from 4.5 to 11.0 m s^{-1}.

The data in figure 13 demonstrate that beneath the wind waves in this study, the influence of microscale wave breaking on the near-surface turbulence extended to a depth of approximately 15 mm. To quantify this influence, the dissipation rates were depth-averaged over the top 15 mm, beneath breaking, $\langle\varepsilon_{msb}\rangle$, and non-breaking waves, $\langle\varepsilon_{non}\rangle$, and these data are shown plotted versus the wind speed in figure 14. For both breaking and non-breaking waves, the depth-averaged dissipation increased approximately linearly with the wind speed. On average $\langle\varepsilon_{msb}\rangle$ was a factor of 1.7 times greater than $\langle\varepsilon_{non}\rangle$ and this factor varied from 1.4 to 2.3 as the wind speed increased from 4.5 to 11 m s^{-1}.

5.3. *Discussion: microscale breaking waves*

Microscale breaking waves are locally generated wind waves that are observed in the laboratory at wind speeds as low as approximately 4 m s^{-1}. Jessup *et al.* (1997) used the time series of the fractional area coverage of microscale breaking waves from infrared imagery to estimate the frequency of occurrence of microscale breaking waves. At a wind speed of 5.0 m s^{-1} and a fetch of 5 m, they estimated that the breaking percentage was 33 %. Banner & Peirson (1998) used a slope threshold to detect microscale breaking waves. They estimated that at a fetch of 4.35 m, 53 %, 70 % and 89 % of the waves break at wind speeds of 4.8, 6.3 and 8.1 m s^{-1}, respectively. The results from these earlier studies and from this study suggest that, even at moderate wind speeds, microscale breaking waves may occupy a significant fraction

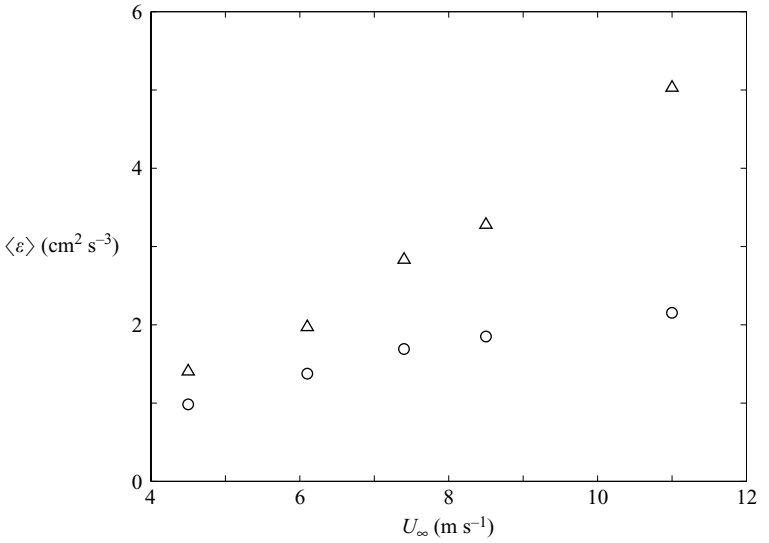

FIGURE 14. The rate of energy dissipation depth-averaged over the top 1.5 cm layer versus wind speed, U_∞. △, $\langle \varepsilon_{msb} \rangle$; ○, $\langle \varepsilon_{non} \rangle$.

of the ocean surface. Field experiments have found that the percentage of large-scale breaking waves (i.e. white caps) ranged from 10 % to 16 % over the wind speed range 8 to 12 m s^{-1} (Holthuijsen & Herbers 1986). Our laboratory results show that over the same range of U_{10}, the percentage of microscale breaking waves varied from 30 % to 80 %, indicating that the frequency of occurrence of microscale breaking waves in the field is much higher than that of large-scale breaking waves.

The resolution of the DPIV data in this study was sufficient for studying the larger-scale processes associated with breaking, in particular the coherent structures. As a wave breaks, the coherent structures first appear immediately upwind of the leading edge and as the breaking process continues, more coherent structures appear and they eventually occupy the entire crest region. As a breaker continues to evolve, additional coherent structures are typically generated (but not always since occasionally only 2–3 coherent structures are observed) until they not only occupy the entire crest region, but also a substantial portion of the upwind face of the advancing breaker (see figure 11). It is evident that as each coherent structure is generated, it quickly begins to decelerate and the speed at which it is advected horizontally is less than the speed of the wave crest or that of the leading edge of the breaker. As a result, the coherent structures are left behind in the water as the breaker advances. As each new coherent structure is generated, during the breaking process, it appears just upwind of the leading edge and immediately downwind of the previously generated coherent structure. This process typically produces a layer of well-mixed fluid with a horizontal length scale equal to approximately the wavelength of the wave (see figure 11*d*) and a depth of the order of the wave height. This well-mixed layer of fluid is visible in the IR images as a region of warmer fluid since the intense mixing associated with the coherent structures disrupts the cool skin layer and exposes warmer bulk fluid at the water surface.

The leading edge of the breaker is clearly visible in the IR images because a relatively sharp temperature gradient occurs across the leading edge (see figure 11). This gradient exists because upwind of the leading edge, the coherent structures have

disrupted the cool skin layer and mixed it with warmer bulk fluid. Downwind of the leading edge, the near-surface fluid is relatively quiescent and hence the cool skin layer (i.e. the thermal boundary layer) is thicker in this region resulting in cooler surface temperatures. Consequently, a temperature gradient is typically observed across the leading edge of breaking waves (see figure 11).

The observed behaviour of the wakes is consistent in the IR images and the DPIV data. The coherent structures are typically strongest (i.e. highest vorticity) near the leading edge and they become weaker moving upwind. Thus, the turbulence is most intense immediately upwind of the leading edge of an actively breaking wave and in this region the wakes in the IR images have the most uniform temperatures because the cool skin layer has been completely disrupted. Moving upwind from the leading edge, the strength of the turbulent motions diminishes and the appearance of the wakes in the IR images become less uniform. That is, small cool patches are now interspersed in the warm wake. At the upwind edge of the wake, the turbulence is weakest and here small warm patches are now interspersed within the cool region outside the wake. These cool regions typically appear here because as the turbulence weakens, the thermal sublayer or cool skin layer thickens. This qualitative description of microscale wave breaking is based on a comprehensive review of the complete DPIV and IR datasets.

Peirson & Banner (2003) argue that the wakes that were observed on the upwind faces of microscale breaking waves were not produced by near-surface turbulence but by weak surface divergence associated with reattachment of the airflow on the upwind faces of the waves (Okuda 1982; Csanady 1990). The coherent structures that we observed in the DPIV data (both in the crest of the waves and on the upwind faces) invariably coincided with the occurrence of a thin thermal sublayer (i.e. a thermal wake) in the IR images. It seems unlikely that a process other than the near-surface turbulence associated with the coherent structures produced the wakes.

This description of the generation and evolution of coherent structures observed beneath microscale breaking waves is consistent with results reported recently by Iafrati & Campana (2005). They numerically modelled the unsteady flow beneath microbreakers generated by a submerged hydrofoil and found that instabilities of the shear flow initially develop between the fluid inside the bulge and the upslope flow. These instabilities lead to the formation of coherent structures which interact with the free surface and induce free-surface fluctuations. At a later stage, the interaction between the vorticity and free-surface curvature induces additional coherent structures that are shed into the water, forming vortex pairs. A plot of the vorticity contours beneath a microscale breaking wave at a wind speed of $11\,\mathrm{m\,s^{-1}}$ is displayed in figure 15. A series of strong near-surface vortices occur upwind of the leading edge of the breaker and the structure of this flow is similar to the flows predicted by Iafrati & Campana (2005), particularly the flow shown in their figure 22.

Peirson & Banner (2003) have reported vorticity magnitudes as high as $200\ \mathrm{s^{-1}}$ upwind of the leading edge of breakers. The spatial resolution of our velocity data is lower than that of Peirson & Banner (2003) and as a result, the localized regions of high vorticity and surface convergence that they observed were not resolved in our DPIV measurements. Nonetheless, we did observe vorticity levels as high as $100\,\mathrm{s^{-1}}$ in the crest regions and on the upwind faces of breaking waves. The vorticity field in figure 15 does have regions of high vorticity behind the leading edge, similar to the observations of Peirson & Banner (2003). The plot also shows that this enhanced vorticity layer extended from the forward face into the wave crest region. Okuda (1982) also observed high vorticity beneath the crests of wind waves. He found

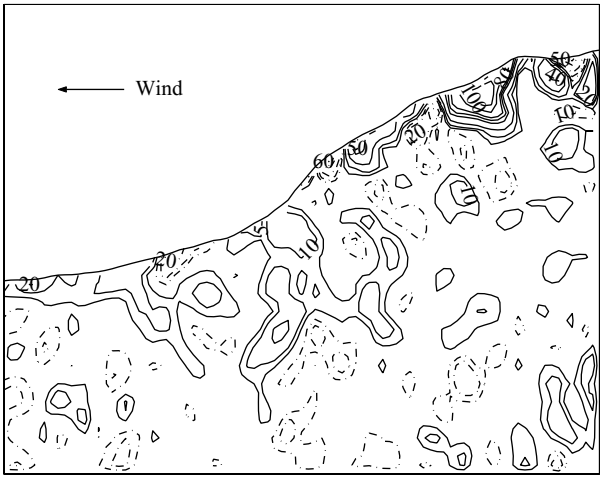

FIGURE 15. The vorticity field on the leeward side of a microscale breaking wave at a wind speed of 11.0 $m\,s^{-1}$. Solid contours correspond to counterclockwise vorticity and dash-dotted contours correspond to clockwise vorticity.

vorticity levels up to $40\,s^{-1}$ beneath wave crests at a wind speed of $5\,m\,s^{-1}$. By comparison, at a wind speed of $4.5\,m\,s^{-1}$, we observed that the average maximum vorticity beneath the wave crests was $20\,s^{-1}$.

The exact nature of the mechanism that is the initial source of the high vorticity in the crest region is not well understood. Longuet-Higgins (1992) argued that the vorticity shed from the troughs of capillary waves is the source of the observed vorticity in the wave crest. Okuda (1982) suggested that the tangential stress is an essential factor for the generation of high vorticity in the crest region. Komori, Nagaoso & Murakami (1993) contended that strong shear produced by organized motions in the air is responsible for the induction of turbulent structures beneath a wave. Peirson & Banner (2003) attributed the high levels of vorticity that they observed at the leading edge of microscale breaking waves to subduction of flow beneath the spilling region. The question of how vorticity is generated at the leading edge of breaking wind waves will remain unanswered until experimental or numerical data with very high spatial and temporal resolution becomes available.

Thais & Magnaudet (1996) measured the bursting frequency of turbulent structures beneath wind ruffled mechanical waves as a function of phase. They found that the bursting frequency in the crest region was more than a factor of four higher than in the trough region and they proposed that micro-breaking was responsible for this phenomenon. Their observations and proposition are consistent with the measurements presented in this study and with our description of the generation of coherent structures by microscale breaking waves. In addition, the downward bursting process observed by Ebuchi, Kawamura & Toba (1993) in which the bursts originated from the wave crest on the leeward face is also consistent with this study and was probably associated with microscale wave breaking. The strong coherent structures and intense turbulence observed beneath the crests of waves of micro-breakers in this study are also consistent with some recent field measurements. Gemmrich & Farmer (2004) found that the rates of dissipation measured beneath the crests of breaking ocean waves were approximately 1.6 times larger than beneath the troughs.

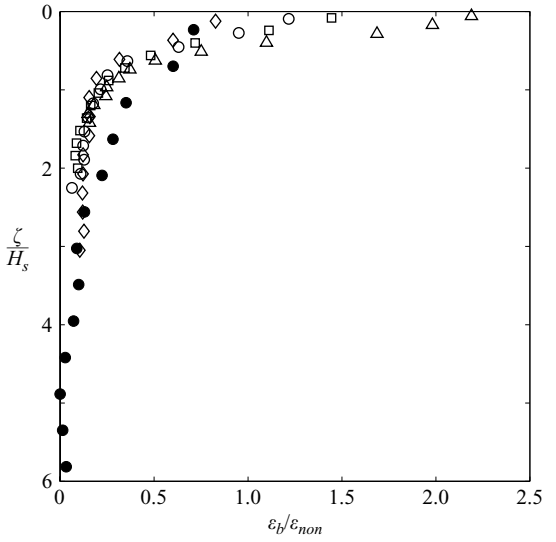

FIGURE 16. The ratio of the rate of energy dissipation due to wave breaking (ε_b) and non-breaking waves (ε_{non}) versus normalized depth, ς/H_s. ●, 4.5 m s^{-1}; ◇, 6.1 m s^{-1}; ○, 7.4 m s^{-1}; □, 8.5 m s^{-1}; △, 11.0 m s^{-1}.

The strong coherent structures that appear beneath the crests of microscale breaking waves produce more intense turbulence than beneath non-breaking waves. This was clearly evident in figures 13 and 14 which showed that beneath microscale breaking waves the rate of dissipation was 1.4 to 2.3 times higher than beneath non-breaking waves. A direct measure of the influence of wave breaking on the turbulence can be obtained by computing the rate of energy dissipation due solely to wave breaking, ε_b, as,

$$\varepsilon_b = \varepsilon_{msb} - \varepsilon_{non}, \tag{8}$$

where, ε_{msb} is the rate of dissipation beneath microscale breaking waves and ε_{non} is the rate of dissipation beneath non-breaking waves. Note that profiles of ε_{msb} and ε_{non} were presented previously in figure 13. The relative contribution of wave breaking to turbulence generation can be quantified using the ratio $\varepsilon_b/\varepsilon_{non}$, where it has been assumed that ε_{non} is not affected by wave breaking. This assumption is an approximation since residual turbulence generated by earlier breaking events may still have been present when a non-breaking wave passed over the measurement location. However, this residual turbulence should be relatively weak, and therefore, the ratio $\varepsilon_b/\varepsilon_{non}$ is a reasonable first-order estimate of the influence of wave breaking on the near-surface turbulence. In figure 16, $\varepsilon_b/\varepsilon_{non}$ is plotted versus the normalized depth, ζ/H_s, for all wind speeds. The plot shows that immediately beneath the water surface the ratio $\varepsilon_b/\varepsilon_{non}$ increased from 0.7 to 2.2 as the wind speed increased from 4.5 to 11 m s^{-1}. This is consistent with the percentage of breaking waves increasing from 11 % to 90 % (see figure 12) over the same wind speed range. It is also evident in figure 16 that the influence of wave breaking on the turbulence extends to a depth of approximately one significant wave height. For $\zeta/H_s > 1.0$, the relative contribution of wave breaking to the turbulence has dropped to less than 30 % (i.e. $\varepsilon_b/\varepsilon_{non} < 0.3$), and for $\zeta/H_s > 3.0$ the contribution is less than 10 %. In figure 9, it was shown that the average rate of dissipation beneath all waves was significantly larger than that

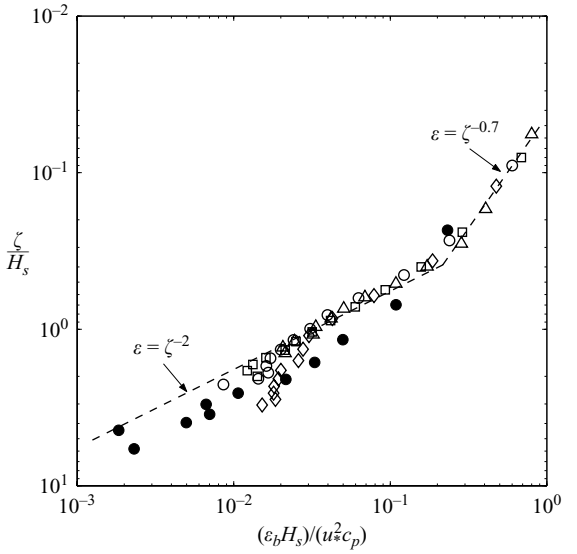

FIGURE 17. The normalized rate of dissipation due to wave breaking, $(\varepsilon_b H_s)/(u_*^2 c_p)$, plotted versus the normalized depth, ς/H_s. ●, 4.5 m s^{-1}; ◇, 6.1 m s^{-1}; ○, 7.4 m s^{-1}; □, 8.5 m s^{-1}; △, 11.0 m s^{-1}.

predicted for a comparable wall layer. The results in figure 16 provide quantitative evidence that this enhanced near-surface dissipation is due to wave breaking.

Terray *et al.* (1996; hereinafter referred to as T) proposed that, in the water column beneath breaking waves, the rate of dissipation scales with the friction velocity, significant wave height, phase speed and the depth. In addition, they argued that ε decayed at three different rates depending on the depth. They assumed that immediately beneath the water surface there is a layer that is directly influenced by wave breaking and in this layer ε is approximately constant. They proposed that a transition layer exists below this layer in which ε decays as z^{-2}, where z is the depth below the mean water level. They claimed that the dissipation rate below the transition layer should exhibit wall-layer behaviour and decay as z^{-1}. The values of ε_b normalized using T's scaling, $\varepsilon_b H_s/u_*^2 c_p$, are plotted in figure 17 for all wind speeds and the data collapse quite well indicating that this scaling is appropriate for ε_b. Note that T's scaling was also applied to profiles of ε, ε_{msb} and ε_{non} and it was found that this scaling did not collapse any of these forms of the dissipation data as well as it did for ε_b. It is evident in figure 17 that two layers exist in which the depth dependence of ε is distinctly different. In the top layer, ε_b decays as $\zeta^{-0.7}$ which does not agree with T's hypothesis that it will be constant. The data in figure 17 indicate that the thickness of the top layer is approximately 0.4 H_s which is in reasonable agreement with T's approximate estimate of 0.6 H_s.

In the transition layer, the data in figure 17 demonstrate that ε decays as ζ^{-2} which is in agreement with T's findings. They argued that the depth of the transition layer depends on the wave age and estimated that its thickness ranged from 8.3 H_s to 13 H_s for their field data. The wind waves in the present study are young with wave ages c_p/u_{*a} in the range 1.0 to 2.0 compared to wave ages of 4.3 to 7.4 for the data used to produce T's figure 7. Using these wave ages in their equation (11) for the thickness of the transition layer, we estimated that beneath these young wind waves

the transition-layer thickness was 3.6 H_s to 7.2 H_s, which is consistent with the data in figure 17.

The magnitude of the normalized dissipation data in figure 17 is approximately an order of magnitude smaller than T's field data. They proposed that the following equation applies in the transition layer,

$$\frac{\varepsilon_b H_s}{u_*^2 c_p} = A\left(\frac{\varsigma}{H_s}\right)^{-2}, \tag{9}$$

where, A is a constant. T's field data, with wave ages in the range 4.3 to 7.4, were used to estimate $A = 0.3$. The data presented in figure 17 were used to estimate that $A = 0.035$, indicating that the coefficient A in (9) is a strong function of wave age. As mentioned earlier, T's scaling collapsed only ε_b within a narrow band. This indicates that T's scaling is applicable to the dissipation associated with microscale wave breaking. That is, the rate of turbulent kinetic energy dissipation due to wave breaking is a function of depth, friction velocity, wave height and phase speed. The collapse of the field dissipation data in T using this scaling confirms that the dissipation rate measured in their experiments was primarily associated with wave breaking.

The data in figure 16 clearly showed that wave breaking significantly enhances the near-surface turbulence, particularly within a depth of one significant wave height. The question of whether this turbulence significantly raises air–water gas transfer rates can be addressed by reviewing the results from Siddiqui *et al.* (2004). In that study, the DPIV velocity data from these experiments was used to investigate the properties of near-surface coherent structures and their influence on air–water gas transfer. The rate of energy dissipation was computed inside and outside the regions occupied by the coherent structures. It was found that the rate of dissipation inside the regions occupied by the coherent structures was 2.5 times larger than that in the regions not occupied by coherent structures. A novel method for estimating the air–water gas transfer velocity based on the surface renewal model was developed. The maximum value of the vorticity of each coherent structure was used to compute the time scale of surface renewal. The gas transfer velocities predicted using this method were in reasonable agreement with measured values. The model predicted that the gas transfer velocity in the regions occupied by coherent structures was enhanced by a factor of 2.8 and contributed 60 % of the total air–water gas flux. Since the majority of the strong coherent structures were generated beneath microscale breaking waves, the results from Siddiqui *et al.* (2004) support the argument that the wakes generated by microscale breaking waves are regions of intense turbulence, which are responsible for the enhancing air–water gas transfer rates. Further evidence in support of this argument is found in the results of Zappa *et al.* (2004) who found that the heat transfer velocities inside the wakes generated by microscale breaking waves were 3.5 times larger than those measured outside the wakes.

Donlon *et al.* (1999) compared the difference in the sea surface skin temperature and the subsurface temperature at various wind speeds and found that at $U_{10} > 6\,\mathrm{m\,s^{-1}}$, the skin temperature was approximately equal to the subsurface temperature. This suggests that at wind speeds greater than $6\,\mathrm{m\,s^{-1}}$, the skin layer at the sea surface disappears. We observed that at $U_{10} \sim 6\,\mathrm{m\,s^{-1}}$ (i.e. $U > 4.5\,\mathrm{m\,s^{-1}}$), the percentage of microscale breaking waves is 10 % (figure 12) and that these breakers enhance the turbulence at the surface by ~70 % (figure 16). Both the percentage of wave breaking and the fraction of the near-surface turbulence produced by wave breaking increased drastically as U_{10} increased from $6\,\mathrm{m\,s^{-1}}$ to $11\,\mathrm{m\,s^{-1}}$. Therefore, a plausible explanation

for the disappearance of the skin layer at wind speeds greater than $6\,\mathrm{m\,s^{-1}}$ is the enhanced near-surface turbulence associated with microscale breaking waves.

6. Conclusions

In this study, the properties of the flow in the aqueous boundary layer formed beneath short wind waves were investigated. Specifically, the similarities and differences of this flow to the flows that occur in conventional wall layers were examined. The only similarity observed was that the mean velocity profiles are logarithmic in both flows. At all wind speeds, beneath these short-fetch wind waves, the aqueous boundary layer was found to be hydrodynamically smooth. However, at significantly longer fetches in the field or laboratory, the aqueous boundary layer will probably be hydrodynamically rougher, that is, in the transition or rough regimes.

The turbulence in the aqueous boundary layer did not display any other similarities to wall-layer turbulence. The rate of dissipation of turbulent kinetic energy was found to be significantly greater than would occur in a comparable wall-layer and to have a different functional dependence on the depth (see figure 9). Microscale wave breaking was found to be responsible for this enhanced near-surface turbulence. Microscale breaking waves were detected and the characteristics of breaking and non-breaking waves were compared. The percentage of microscale breaking waves increased abruptly from 11 % to 80 % as the wind speed increased from 4.5 to $7.4\,\mathrm{m\,s^{-1}}$ and then gradually increased to 90 % as the wind speed increased to $11\,\mathrm{m\,s^{-1}}$. At a depth of 1 mm, the rate of dissipation was found to be 1.7 to 3.2 times greater beneath microscale breaking waves than beneath non-breaking waves. In the crest–trough region beneath microscale breaking waves, 40 % to 50 % of the dissipation is associated with wave breaking.

In a conventional wall layer, the rate of dissipation is a function of only the friction velocity and the distance from the wall, that is, $\varepsilon = f(u_*, z)$. However, beneath a wind-driven air–water interface, the turbulence generated by large-scale breaking waves (i.e. whitecaps) is also a function of the wave properties (T). This was also shown to be true for the turbulence generated beneath microscale breaking waves in figure 17 where it was demonstrated that, $\varepsilon_b = f(u_*, \varsigma, H_s, c_p)$. Figure 17 also showed that ε_b does not decays as ς^{-1}, as would be expected in a wall layer, but that there are two distinct layers; an upper layer where $\varepsilon_b \sim \varsigma^{-0.7}$and a lower layer where $\varepsilon_b \sim \varsigma^{-2}$. The enhanced turbulence associated with microscale wave breaking was found to extend to a depth of approximately one significant wave height (see figure 16). These two figures provide clear evidence that microscale wave breaking is the mechanism responsible for the intense near-surface turbulence observed in the crest-trough region (i.e. $\zeta < H_s$). Microscale wave breaking can be thought of as intense wave–turbulence interactions that lead to the production of turbulence in the crest–trough region as was proposed by Thais & Magnaudet (1996).

A detailed examination of our unique DPIV data set and the simultaneously sampled IR image sequences provided us with improved knowledge about the characteristics of microscale breaking and non-breaking waves and also led to new insights into the process of microscale wave breaking. The differences that we observed between microscale breaking and non-breaking waves are summarized schematically in figure 18. Microscale breaking waves are steeper and larger in amplitude than non-breaking waves. The occurrence of a microscale breaking wave always results in the production of strong coherent structures that appear upwind of the leading edge of the breaker. A typical microscale breaking wave produces a number of coherent

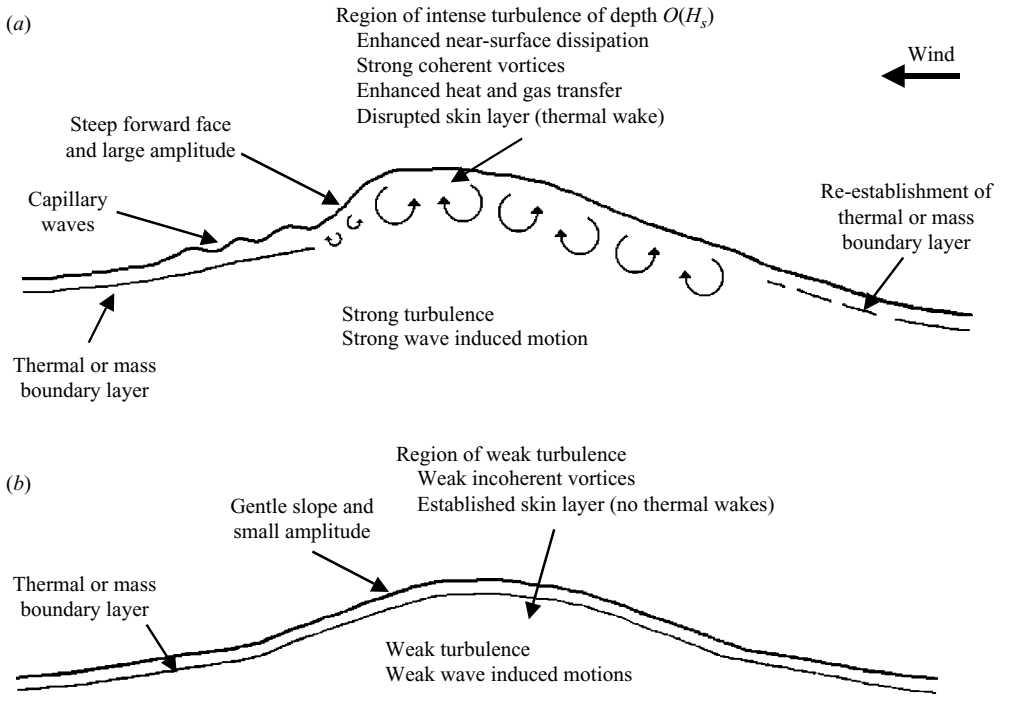

FIGURE 18. Schematic diagram illustrating the differences between (*a*) microscale breaking waves, and (*b*) non-breaking waves. The diagram is not to scale.

structures which disrupt the thermal and/or mass boundary layers creating a patch of well-mixed fluid (i.e. a wake) with a horizontal dimension of the order of a wavelength and a depth of the order of the significant wave height. These well-mixed patches of fluid are regions of enhanced near-surface turbulence that produce the warm wakes that are visible in the IR images. Inside these wakes, the rate of heat and gas transfer has been shown to be considerably enhanced because of the energetic mixing produced by the near-surface turbulence generated by microscale wave breaking. As the turbulent wake subsides, the disrupted boundary layer re-establishes itself. By comparison the turbulence beneath the crests of non-breaking waves is comprised of relatively weak incoherent vortices that are typically not strong enough to disrupt the thermal or mass boundary layers. Consequently, the rate of heat and gas transfer across the surface of non-breaking waves is significantly lower than that across microscale breaking waves.

A. T. Jessup and W. E. Asher collaborated closely with us in conducting these experiments and without their expertise this work would not have been possible. In addition, we thank Chris Zappa and Christine Richardson for their assistance with the IR measurements. This research was funded by a grant from the Natural Sciences and Engineering Research Council of Canada to M. R. L.

REFERENCES

AGRAWAL, Y. C., TERRAY, E. A., DONELAN, M. A., HWANG, P. A., WILLIAMS III, A. J., DRENNAN, W. M., KAHMA, K. K. & KITAIGORODSKII, S. A. 1992 Enhanced dissipation of kinetic energy beneath surface waves. *Nature*. **359**, 219–220.

Anis, A. & Moum, J. N. 1995 Surface wave–turbulence interactions – scaling epsilon (z) near the sea-surface. *J. Phys. Oceanogr.* **25**, 2025–2045.

Banner, M. L. & Peirson, W. L. 1998 Tangential stress beneath wind-driven air–water interfaces. *J. Fluid Mech.* **364**, 115–145.

Banner, M. L. & Peregrine, D. H. 1993 Wave breaking in deep water. *Annu. Rev. Fluid Mech.* **25**, 373–397.

Banner, M. L. & Phillips, O. M. 1974 On the incipient breaking of small scale waves. *J. Fluid Mech.* **65**, 647–656.

Benilov, A. Yu, Kouznetsov, O. A. & Panin, G. N. 1974 On the analysis of wind-induced disturbances in the atmospheric turbulent surface layer. *Boundary-Layer Met.* **6**, 269–285.

Bock, E. J., Hara, T., Frew, N. M. & McGillis, W. R. 1999 Relationship between air–sea gas transfer and short wind waves. *J. Geophys. Res.* **104**, 25821–25831.

Bourassa, M. A. 2000 Shear stress model for the aqueous boundary layer near the air–sea interface. *J. Geophys. Res.* **105(C1)**, 1167–1176.

Bye, J. A. T. 1965 Wind-driven circulation in unstratified lakes. *Limnol. Oceanogr.* **10**, 451–458.

Bye, J. A. T. 1967 The wave-drift current. *J. Marine Res.* **25**, 95–102.

Cheung, T. K. & Street, R. L. 1988 The turbulent layer in the water at an air–water interface. *J. Fluid Mech.* **194**, 133–151. (Referred to herein as CS).

Churchill, J. H. & Csanady, G. T. 1983 Near-surface measurements of quasi-Lagrangian velocities in open water. *J. Phys. Oceanogr.* **13**, 1669–1680.

Csanady, G. T. 1990 The role of breaking wavelets in air–sea gas transfer. *J. Geophys. Res.* **95**, 749–759.

Donelan, M. A. 1990: Air–Sea Interaction. The Sea: Ocean Engineering Science, vol. 9 (ed. B. LeMéhauté & D. Hanes), pp. 239–292. John Wiley.

Donlon, C. J., Nightingale, T. J., Sheasby, T., Turner, J., Robinson, I. S. & Emery, W. J. 1999 Implications of the oceanic thermal skin temperature deviation at high wind speed. *Geophys. Res. Lett.* **26**, 2505–2508.

Doron, P., Bertuccioli, L., Katz, J. & Osborn, T. R. 2001 Turbulence characteristics and dissipation estimates in the coastal ocean bottom boundary layer from PIV data. *J. Phys. Oceanogr.* **31**, 2108–2134.

Ebuchi, N., Kawamura, H. & Toba, Y. 1993 Bursting phenomena in the turbulent boundary layer beneath the laboratory wind-wave surface. Natural Physical Sources of Underwater Sound (ed. B. R. Kerman) pp. 263–276.

Frew, N. M., Bock, E. J., Schimpf, U., Hara, T., Haussecker, H., Edson, J. B., McGillis, W. R., Nelson, R. K., McKenna, S. P., Uz, B. M. & Jähne, B. 2004 Air–sea gas transfer: its dependence on wind stress, small-scale roughness, and surface films. *J. Geophys. Res.* **109**, C08S17, 1–23.

Gemmrich, J. R. & Farmer, D. M. 2004 Near-surface turbulence in the presence of breaking waves. *J. Phys. Oceanogr.* **34**, 1067–1086.

Hinze, J. O. 1975 *Turbulence*. McGraw–Hill.

Holthuijsen, L. H. & Herbers, T. H. C. 1986 Statistics of breaking waves observed as whitecaps in the open sea. *J. Phys. Oceanogr.* **16**, 290–297.

Hsu, C.-T., Hsu, E. Y. & Street, R. L. 1981 On the structure of turbulent flow over a progressive water wave: theory and experiment in a transformed, wave-following coordinate system. *J. Fluid Mech.* **105**, 87–117.

Iafrati, A. & Campana, E. F. 2005 Free-surface fluctuations behind microbreakers: space–time behaviour and subsurface flow field. *J. Fluid Mech.* **529**, 311–347.

Jähne, B., Munnich, K. O., Bosinger, R., Dutzi, A., Huber, W. & Libner, P. 1987 On the parameters influencing air–water gas exchange. *J. Geophys. Res.* **92**, 1937–1949.

Jessup, A. T., Zappa, C. J. & Yeh, H. 1997 Defining and quantifying microscale wave breaking with infrared imagery. *J. Geophys. Res.* **102**, 23 145–23 153.

Jiang, J.-Y., Street, R. L. & Klotz, S. P. 1990 A study of wave–turbulence interaction by use of a nonlinear water wave decomposition technique. *J. Geophys. Res.* **95**, 16 037–16 054.

Jiménez, J. 2004 Turbulent flow over rough walls. *Annu. Rev. Fluid Mech.* **36**, 173–196.

Kahma, K. K. & Donelan, M. A. 1988 A laboratory study of the minimum wind speed for wind wave generation. *J. Fluid Mech.* **192**, 339–364.

Keulegan, G. H. 1951 Wind tides in small closed channels. *J. Res. Nat. Bur. Stand.* **46**, 358–381.

Kitaigorodskii, S. A., Donelan, M. A., Lumley, J. L. & Terray, E. A. 1983 Wave–turbulence interactions in the upper ocean. Part II: Statistical characteristics of wave and turbulent components of the random velocity field in the marine surface layer. *J. Phys. Oceanogr.* **13**, 1988–1999.

Komori, S., Nagaosa, R. & Murakami, Y. 1993 Turbulence structure and mass transfer across a sheared air–water interface in wind-driven turbulence. *J. Fluid Mech.* **249**, 161–183.

Kundu, P. K. & Cohen, I. M. 2002 *Fluid Mechanics.* Academic.

Law, C. N. S., Khoo, B. C. & Chew, T. C. 1999 Turbulence structures in the immediate vicinity of the shear-free air–water interface induced by a deeply submerged jet. *Exps. Fluids* **27**, 321–331.

Lin, J. T. & Gad-El-Hak, M. 1984 Turbulent current measurements in a wind wave tank. *J. Geophys. Res.* **89**, 627–636.

Loewen, M. R. & Siddiqui, M. H. K. 2006 Detecting microscale breaking waves. *Meas. Sci. Technol.* **17**, 771–780.

Longuet-Higgins, M. S. 1992 Capillary rollers and bores. *J. Fluid Mech.* **240**, 659–679.

Makin V. K. & Kudryavtsev, V. N. 2002 Impact of dominant waves on sea drag. *Boundary-Layer Met.* **103**, 83–99.

Mei, C. C. 1983 The applied dynamics of ocean surface waves. Wiley-Interscience.

Melville, W. K. 1994 Energy dissipation by breaking waves. *J. Phys. Oceanogr.* **24**, 2041–2049.

Melville, W. K. 1996 The role of surface-wave breaking in air–sea interaction. *Annu. Rev. Fluid Mech.* **28**, 279–321.

Melville, W. K., Veron, F. & White, C. J. 2002 The Velocity field under breaking waves: coherent structures and turbulence. *J. Fluid Mech.* **454**, 203–233.

Okuda, K. 1982 Internal flow structures of short wind waves. I. On the internal vorticity structures. *J. Oceanogr. Soc. Japan* **38**, 28–42.

Peirson, W. L. 1997 Measurements of surface velocities and shear at a wavy air–water interface using particle image velocimetry. *Exps. Fluids* **23**, 427–437.

Peirson, W. L. & Banner, M. L. 2003 Aqueous surface layer flows induced by microscale breaking wind waves. *J. Fluid Mech.* **479**, 1–38.

Schlichting, H. T. & Gersten, K. 2000 *Boundary-Layer Theory*. McGraw–Hill.

Shemdin, O. H. 1972 Wind-generated current and phase speed of wind waves. *J. Phys. Oceanogr.* **2**, 411–419.

Siddiqui, M. H. K., Loewen, M. R., Richardson, C., Asher, W. E. & Jessup, A. T. 2001 Simultaneous particle image velocimetry and infrared imagery of microscale breaking waves. *Phys. Fluids* **13**, 1891–1903.

Siddiqui, M. H. K., Loewen, M. R., Asher, W. E. & Jessup, A. T. 2004 Coherent structures beneath wind waves and their influence on air–water gas transfer. *J. Geophys. Res.* **109**, C3, C03024.

Sirovich, L. & Karlsson, S. 1997 Turbulent drag reduction by passive mechanisms. *Nature* **388**, 753–755.

Smith, S. D. 1988 Coefficients for sea surface wind stress, heat flux, and wind profiles as a function of wind speed and temperature. *J. Geophys. Res.* **93(C12)**, 15 467–15 472.

Soloviev, A. & Lukas, R. 2003 Observation of wave-enhanced turbulence in the near-surface layer of the ocean during TOGA COARE. *Deep-Sea Res.* I, **50**, 371–395.

Soloviev, A. V., Vershinsky, N. V. & Bezverchinii, V. A. 1988 Small-scale turbulence measurements in the thin surface layer of the ocean. *Deep-Sea Res.* **35**, 1859–1874.

Sullivan, P. P., McWilliams, J. C. & Melville, W. K. 2004 The oceanic boundary layer driven by wave breaking with stochastic variability. Part 1. Direct numerical simulations. *J. Fluid Mech.* **507**, 143–174.

Tennekes, H. & Lumley, J. L. 1972 *A First Course in Turbulence.* MIT press.

Terray, E. A., Donelan, M. A., Agrawal, Y. C., Drennan, W. M., Kahama, K. K., Williams, III, A. J., Hwang, P. A. & Kitaigorodskii, S. A. 1996 Estimates of kinetic energy dissipation under breaking waves. *J. Phys. Oceanogr.* **26**, 792–807. (Referred to herein as T).

Thais, L. & Magnaudet, J. 1995 A triple decomposition of the fluctuating motion below laboratory wind water-waves. *J. Geophys. Res.* **100(C1)**, 741–755.

Thais, L. & Magnaudet, J. 1996 Turbulent structure beneath surface gravity waves sheared by the wind. *J. Fluid Mech.* **328**, 313–344.

Turner, J. S. 1973 *Buoyancy Effects in Fluids*. Cambridge University Press.

Van Dorn W. G. 1953 Wind Stress on an Artificial Pond. *J. Mar. Res.* **12**, 249–276.

Veron, F. & Melville, W. K. 1999 Pulse-to-pulse coherent Doppler measurements of waves and turbulence. *J. Atmos. Oceanic. Technol.* **16**, 1580–1597.

Wu, J. 1975 Wind-induced drift currents.*J. Fluid Mech.* **68**, 49–70.

Zappa, C. J., Asher, W. E. & Jessup, A. T. 2001 Microscale wave breaking and air–water gas transfer. *J. Geophys. Res.* **106**, 9385–9391.

Zappa, C. J., Asher, W. E., Jessup, A. T., Klinke, J. & Long, S. R. 2004 Microbreaking and the enhancement of air–water gas transfer velocities. *J. Geophys. Res.* **109**, C8, C08S16.